



Translational Inertial Effects and Scaling Considerations for Coarse Granular Flows Impacting Landslide-Resisting Barriers

George Robert Goodwin, Ph.D.¹; and Clarence Edward Choi, Ph.D.²

Abstract: Coarse grains accumulate at granular flow fronts and must be considered when studying granular flows impacting barriers. Experimental studies often use instrumented barriers comprising a load transducer and load-bearing plate. However, it is not clear how to scale the mass of these composite barriers relative to coarse grains such that forces induced are properly captured by the load transducer. This study considers the impact force from grains on instrumented barriers using both a physical flume and a discrete element method (DEM) model. Results reveal two main scaling considerations for granular flows impacting load-measuring systems: (1) the design of the load-measuring system, and (2) the model size. Considerations relating to the design of the load-measuring system include (1) the relative mass of the grains and the load-measuring system; (2) the spring element stiffness of the load-measuring system; and (3) the grain impact velocity. These are captured using a newly proposed dimensionless number. Additionally, discrete impacts appear to reduce in importance as the sizes of the flow and channel are increased, relative to the final static load due to the flow piling up, within the framework of Hertzian impact mechanics. This implies that small-scale DEM simulations adopting low elastic moduli (reducing discrete impact loads) may unintentionally correctly represent larger-scale impact dynamics. DOI: [10.1061/\(ASCE\)GT.1943-5606.0002661](https://doi.org/10.1061/(ASCE)GT.1943-5606.0002661). © 2021 American Society of Civil Engineers.

Author keywords: Debris flow impact; Boulder impact; Discrete element method (DEM); Physical load measurements; Impact load scaling.

Introduction

Coarse grains accumulate at the front of channelized granular flows, such as debris flows or rock avalanches. These flow fronts tend to be unsaturated and behave discretely (Baselt et al. 2021). To arrest coarse-grained flow fronts, rigid barriers are often used (NILIM 2007; WSL 2008; Kwan 2012; Piton and Recking 2016a, b; Ng et al. 2018a). A key design consideration is the force that the barriers are required to resist from the coarse frontal grains, which affects the deduced impact coefficients for design purposes (e.g., Kwan 2012). Many small-scale physical studies have been carried out to investigate the impact loads from flow fronts (e.g., Faug et al. 2002, 2003, 2008, 2011; Hákonadóttir et al. 2003a, b; Naaim-Bouvet et al. 2004; Moriguchi et al. 2009; Mancarella and Hungri 2010; Canelli et al. 2012; Jiang and Towhata 2013; Scheidl et al. 2013; Vagnon and Segalini 2016; Ng et al. 2016, 2021; Song et al. 2017; Tan et al. 2020).

Generally speaking, these studies have been successful at capturing areal loads due to continuumlike behavior. For discrete behavior, considerable research has been performed on loading from single impacts from boulders (e.g., Yigit et al. 2011; Spadari et al. 2012; Christoforou et al. 2013; Lam et al. 2018a, b; Ng et al. 2018b; Su et al. 2017, 2018; Yong et al. 2019). However, there are several scale-related challenges that have not been elucidated when trying to

capture discrete loads from the frontmost coarse grains in channelized granular flows. These flows involve successive impacts, collisions among grains, and the concurrent accumulation of static loading.

Load transducers are used for physically measuring loads. These transducers require elastic deformation or displacement (e.g., Kluger et al. 2016; Maranzano and Hancock 2016), which is often characterized as an effective spring element stiffness. For studies on granular flows, load transducers are generally rigidly attached to load-bearing plates, which provide an interface for flow material. However, the mass of these load-bearing plates plays an important role in resisting movement. Depending on the relative mass of the coarse grains and the load-measuring barrier system, the force from the impact may not be fully transmitted as load. This is especially problematic in physical modeling of the impact of coarse granular flow fronts. Some examples of data from physical studies are shown in Fig. 1 (specifically, Jiang and Towhata 2013; Scheidl et al. 2013; Bugnion et al. 2012).

In Fig. 1(a), the test was using dry gravel with diameters in the range $10 < \delta < 25$ mm; the channel inclination was $\theta = 40^\circ$, and the channel width and length were 0.3 and 2.2 m, respectively. The barrier was split vertically into multiple sections, as shown in the inset. Flow velocities were up to 5 m/s. In Fig. 1(b), the test used saturated sediments with a grain-size distribution range of $0.2 \mu\text{m} < \delta < 50$ mm. The width of the channel is 0.45 m. The impact velocity was up to around 2.5 m/s. The time history is for a single load cell at the bottom of the array. In Fig. 1(c), the test used saturated sediments with a well-sorted grain-size distribution in the range of $1 \mu\text{m} < \delta < 80$ mm. The width of the channel is 8 m. Flow velocities were up to around 10 m/s.

In Figs. 1(b and c), both the raw data and filtered data are shown. Given the grain-size distribution adopted in these studies, as well as the apparent levels of ambient electronic noise, it can be inferred that at least some of these peaks are due to discrete impacts. However, it is rather difficult to assess the extent to which forces are transmitted as load because few studies give comprehensive information

¹Institut national de recherche pour l'agriculture, l'alimentation et l'environnement, Grenoble 38100, France; Dept. of Civil Engineering, Univ. of Hong Kong, Pokfulam, Hong Kong SAR. Email: george.goodwin@inrae.fr; cechoi@hku.hk

²Assistant Professor, Dept. of Civil Engineering, Univ. of Hong Kong, Pokfulam, Hong Kong SAR (corresponding author). Email: cechoi@hku.hk

Note. This manuscript was submitted on December 5, 2020; approved on July 1, 2021; published online on September 28, 2021. Discussion period open until February 28, 2022; separate discussions must be submitted for individual papers. This paper is part of the *Journal of Geotechnical and Geoenvironmental Engineering*, © ASCE, ISSN 1090-0241.

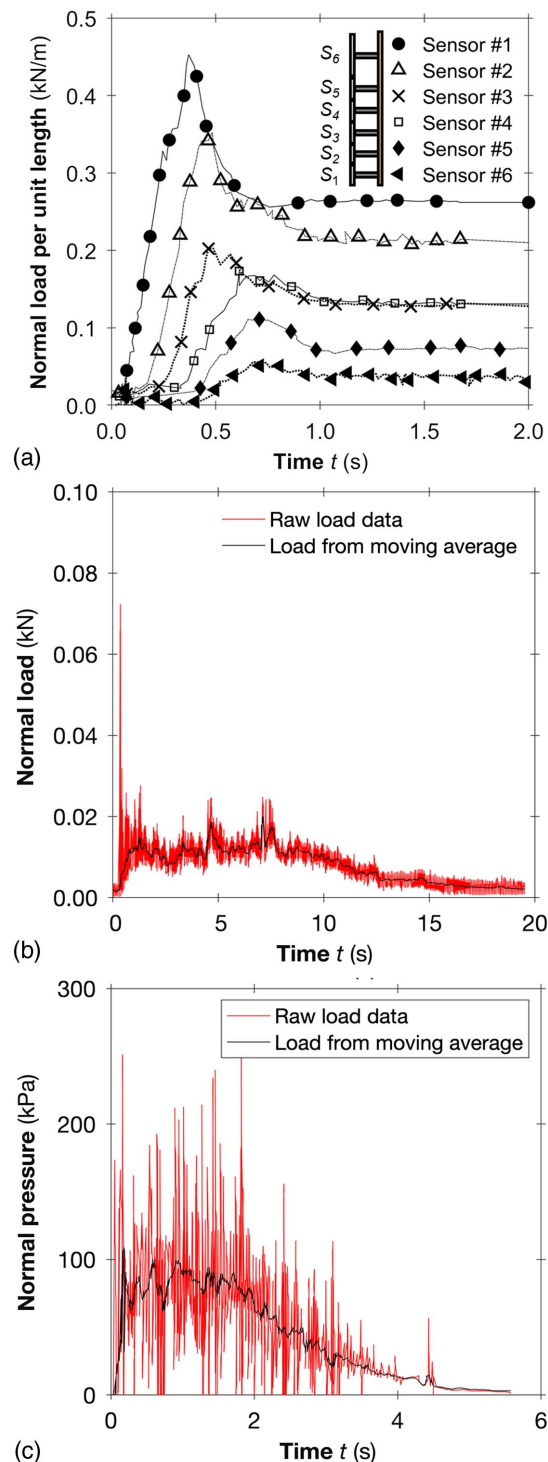


Fig. 1. Some load-time histories from the literature for granular flows impacting barriers, extracted using the software Web Plot Digitizer version 4.3 (Marin et al. 2017) and then replotted: (a) Jiang and Towhata (2013); (b) Scheidl et al. (2013); and (c) Bugnion et al. (2012).

about the design of their load-measuring systems (Table 1). More importantly, these discrete impacts often represent the maximum loads that are used to deduce impact coefficients for design recommendations (Kwan 2012).

Numerical approaches for modeling the impact of granular flows include three-dimensional (3D) finite-element models (Ng et al. 2018a) and the discrete element method (DEM) (e.g., Teufelsbauer et al. 2009, 2011; Law et al. 2015; Leonardi et al. 2019). The DEM is

best placed for explicitly accounting for translational inertial impacts due to individual grains, relevant to coarse granular flow fronts.

We acknowledge that there are both soft-sphere (e.g., Cundall and Strack 1979; Johnson 1985; O'Sullivan 2011), as well as hard-sphere DEM models (e.g., Stratton and Wensrich 2010; Richardson et al. 2011; Murdoch et al. 2012) in addition to hybrid models (e.g., Buist et al. 2016). The difference between soft- and hard-sphere approaches is in the modeling of contact forces. Soft-sphere methods compute contact forces by allowing a certain degree of penetration between particles. In contrast, hard-sphere methods compute when the paths of grains will cross, and mediate the collision with relatively simple formulations based on the transfer of momentum (Murdoch et al. 2012). The advantage of the hard-sphere method is that collisions can be computed cheaply, with only a single calculation required per collision. This is in contrast with soft-sphere methods where intergrain interactions require many time steps to resolve collisions properly. The disadvantage of the hard-sphere method lies in handling multiple simultaneous contacts; the computation of the dynamics of multiple simultaneously interacting bodies across a single timestep may not be trivial. Furthermore, hard-sphere methods are less able to provide realistic treatments of frictional contacts (Murdoch et al. 2012) because contacts are much less likely to be persistent than in soft-sphere approaches.

For the problem of granular flows impacting barriers, it appears that the soft-sphere approach has a clear advantage because persistent frictional contacts can be modeled due to the slight overlap of grains afforded by the contact model. Granular flows are often dense (Jop et al. 2006), and so both frictional contacts and multiple simultaneous contacts are commonplace. Furthermore, flows generally come to rest after impact with closed barriers, with the simultaneous development of a dead zone (e.g., Gray et al. 2003; Hákonadóttir et al. 2003a; Choi et al. 2016; Ng et al. 2017, 2019). Both dense flows and dead zones are clearly governed by persistent multiple contacts and frictional forces, underlining the need for soft-sphere approaches.

Indeed, it is worth emphasizing that all of the DEM studies on the impact of grains or granular flows collected in Table 1 have adopted soft-sphere approaches. This is sufficient motivation for comparing soft-sphere approaches for modeling the impact force of granular flows on barriers at different scales.

In the soft-sphere DEM (Cundall and Strack 1979), grain contacts can be modeled using Hertzian mechanics (Johnson 1985)

$$F_{\text{grain}} = \frac{4}{3} E^* \sqrt{r_g} (d)^{\frac{3}{2}} \quad (1)$$

where E^* = effective elastic modulus corresponding to material stiffness (defined in full in Appendix I); r_g = grain radius; and d = either the elastic deformation or the overlap between grains, depending on how the impact is being modeled. An analytic expression for the maximum value of d can be written (Zhang et al. 1996)

$$d = \left(\frac{15mU_1^2}{16E^* \sqrt{r_g}} \right)^{0.4} \quad (2)$$

where m = grain mass; and U_1 = preimpact velocity. Although the parameters that appear in Eq. (1) can be characterized with clear physical meanings, the input parameters for DEM studies on granular impact vary substantially, even when modeling the same (or similar) geological materials. Table 2 summarizes DEM studies on impact due to granular flows.

Studies that adopt Hertzian contact models (e.g., Shan and Zhao 2014; Law et al. 2015; Ng et al. 2017; Shen et al. 2018) implemented an elastic modulus E ranging from 1×10^{-1} to 7×10^2 GPa. At the lower end of this range, the elastic moduli are much lower than the material parameters that they are supposed to be modeling. Varying

Table 1. Summary of load-measuring system properties for various physical studies

Study	Channel		Load-bearing plates					Load transducer					Granular material			Flow	
	Incl. (degrees)	Width B (m)	No.	H (m)	W (m)	D (m)	Material	Type	H_t (m)	W_t (m)	D_t (m)	Material	Freq. (kHz)	Material	δ_{\min} (mm)	δ_{\max} (mm)	U_{\max} (m/s)
Tiberghien et al. (2007)	0–10	0.3	1	0.02–0.06	0.3	0.02	—	Two load cells (range 2 N)	0.1	0.01	—	—	30	Liquid (Carbopol)	—	—	0.15
Shieh et al. (2008)	6–10	0.2	2	0.3	0.22	0.2	Acrylic	Two load cells (behind and above obstacle)	—	—	—	—	—	Gravel & water	3.6	3.6	2.7
Moriguchi et al. (2009)	45–65	0.30	1	0.30	0.30	0.15	Wood/rubber	Kyowa (Tokyo) LCN-A-5 kN	0.05	0.25	—	—	1	Dry Toyoura sand	0.1	0.4	3.5
Ishikawa et al. (2010)	18	—	1	—	—	—	—	One load cell	—	—	—	—	—	Sand, gravel & water	0.1	20	—
Bugnion et al. (2012) ^a	30	8.00	1	0.16	0.26	—	Steel/elastomer	Cylindrical strain gauge sensor (20 kN)	0.12	—	—	—	2	Mixture	0.001	80	10.4
Caccamo et al. (2012)	21–33	0.25	1	—	0.01	—	—	2 XF3C300 (TE Connectivity, Schaffhouse, Switzerland)	—	—	—	—	1	Dry glass beads	1	1	1.2
Canelli et al. (2012)	30	0.4	1	—	—	—	—	4 load transducers	—	—	—	—	—	Saturated sand	1	1	—
Jiang and Towhata (2013)	30–45	0.30	5	0.05	0.30	—	—	Bending beam	0.03	0.03	0.20	—	—	Angular gravel	10	25	5.0
Scheidl et al. (2013)	17	0.45	24	0.04	0.04	—	—	—	—	—	—	—	2.4	Mixture	0.0002	50	2.5
Ashwood and Hungr (2016)	22–34	0.31	1	0.36	0.31	—	Plywood/sheet metal	Omega (Norwalk, Connecticut) LCCA-1K (453.6 kg) S-beam strain gauge	—	—	—	—	5–6	Dry sand/gravel	0.5	8	3.6
Song (2016) ^b	25	0.23 (5.2)	1	0.2 (4.5)	0.23 (5.2)	0.01	Steel	Donut	—	—	—	—	20	Sand/glass beads	0.6 (13)	39 (1)	13.3

Note: An em-dash indicates information that does not appear to be given in the paper. Incl. = inclination; and freq. = frequency.

^aThe plates include an elastomer layer for dampening impulses.

^bNumbers in brackets indicate nominal dimensions under high- g conditions (25 g).

Table 2. Summary of DEM input parameters for various studies

Property	An and Tannant (2007)	Teufelsbauer et al. (2009)	Salciarini et al. (2010)	Zhou and Ng (2010)	Teufelsbauer et al. (2011)	Shan and Zhao (2014)	Law et al. (2015)	Ng et al. (2017)	Shen et al. (2018)	Marchelli et al. (2019)
No. of grains	—	—	3,000	~15,000	43,000	15,000	65,000	40,000	7,000	8,000
Grain diameter δ (m)	0.1	0.004–0.006	—	0.02–0.08	0.0025	0.07	0.005	0.008	0.005–0.013	0.1
Elastic modulus (N/m ²)	—	—	—	—	—	$7 \times 10^{10}/7 \times 10^{11}$ a	1×10^8	1×10^8	1×10^8	—
Ball norm. stiffness (N/m)	10×10^7	1.2×10^3	1×10^8	1×10^5	1×10^8	—	—	—	—	1×10^5
Ball tang. stiffness	—	—	2.5×10^7	—	—	—	—	—	—	3×10^4
Poisson's ratio	—	0.3	0.33	—	—	0.3	—	—	0.25	—
Ball-ball fric	—	—	16–38	30	35	0.7	35	35	1.3	0.58
Ball-wall fric	—	—	—	—	—	—	—	22.6	0.38	—
CoR	0.2–0.7	0.75	0.42	—	0.5	0.7	0.5	0.5	—	0.8
Density	2,600	2,900	2,650	2,650	N/A	2,700	N/A	2,650	2,500	2,500
No. of dimensions	2	3	2	3	3	3	3	3	3	3
Mean part. overlap	—	1×10^{-8}	—	—	—	—	—	—	—	—
Contact model	Hooke	Hooke	Mono	Hooke	Kelvin–Voigt	Hertz Mono	Hooke Mono	Hertz Mono	Hooke Poly	Hertz Poly
Polydispersity	—	Poly	—	Both	—	0.5	5	5	1	30
Timesstep (μ s)	—	30	—	—	—	—	—	—	—	—

Note: An m-dash indicates information that does not appear to be given in the paper. CoR = coefficient of restitution.

^aShan and Zhao (2014) adopt different elastic moduli for ball-ball and ball-wall, with the latter $10 \times$ that of the former (i.e., 700 GPa).

E does not cause much difference for the bulk flow dynamics of channelized flows (e.g., Kumaran and Bharathraj 2013), but it should affect the discrete forces generated during collisions [Eqs. (1) and (2)].

DEM barriers are usually modeled as being immobile, rather than modeling a load-measuring system explicitly. This means that the DEM ignores the translational movement and imperfect transmission of impact force into measured load that physical load-measuring systems entail. This strongly suggests the presence of compensating error when calibrating numerical models to match physically obtained impact loads (e.g., Cui et al. 2018; Leonardi et al. 2019). This compensating error is partly caused by giving DEM barriers a lower-than-realistic material stiffness. No study has investigated this compensating error for coarse granular flow impacts where successive impacts, collisions among grains, and the concurrent accumulation of static loading through the formation of a dead zone are all important.

Furthermore, because the impact duration is related to the elastic modulus (Leonardi et al. 2014), the possibility of loads from multiple grains being exerted on a barrier simultaneously increases as the elastic modulus decreases. It is currently unclear whether there are any circumstances under which concurrent discrete loads govern flow–structure interaction. Better understanding of these concurrent discrete loads will improve the estimation of impact loads induced on landslide-resisting barriers by granular flows.

Scope of This Study

The literature review has revealed that there is no clear rationale behind the design of physical instrumented barriers for measuring loads due to channelized granular flows. In particular, the mass of the barrier tends to be much higher than that of the impacting grains, which causes impact forces to be imperfectly transmitted as measured loads. There has been no investigation of how to optimize the ratio of the masses of the barrier and impacting grains such that true loads can be obtained, either at laboratory scale or field scale.

The literature review has also revealed that the soft-sphere DEM is often adopted for studies on channelized granular flows impacting barriers. Collectively, the ultimate long-term goal of these studies is to devise a generalizable impact model that can be used for engineering design. However, scaling effects relating to soft-sphere contact models, and the input parameters that these models require, have not been explored in the literature.

In this study, data from six new physical flume experiments and a DEM model implementing Hertzian contact mechanics are compared in order to address these challenges.

Initially, we address the problem of scaling the translational inertia of physical instrumented barriers, such that dynamic loads from the fronts of coarse granular flows can be measured. We do this using physical and DEM drop tests involving a single particle and a load-transducer system. A parametric study is carried out in which both the spring element stiffness and the material stiffness are varied, modeling the key parameters of a load-measuring system.

We then investigate for the first time scaling effects for Hertzian soft-sphere contact models in the context of the impact of channelized granular flows. A series of six physical granular flow impact tests using an instrumented barrier are conducted, covering a range of Froude numbers Fr . Corresponding DEM simulations are then run varying the material stiffness, which is often artificially reduced for numerical convenience in studies in the literature. This is the first systematic investigation of input parameters for Hertzian

soft-sphere models in the context of determining peak impact loads for granular flows. Further simulations are run to understand the effects of scale. These scaling effects must necessarily be understood before using numerical tools to tackle large-scale engineering problems, such as computing the peak forces on barriers due to coarse granular flows.

Methodology: Single-Grain Drop Tests

Physical Modeling Procedure

A drop-test apparatus was used for this study (Fig. 2). This physical equipment has previously been used by Ng et al. (2019). A load cell transducer with a nominal range of 5 kN was fixed 0.5 m beneath a

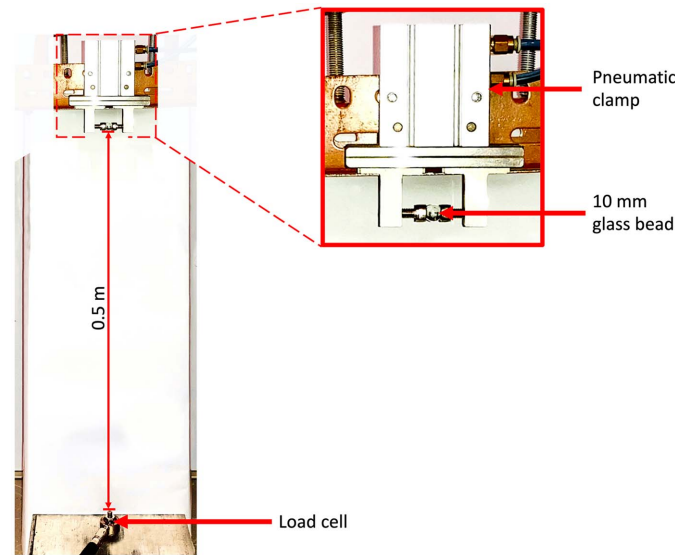


Fig. 2. Drop test apparatus. The drop distance was 0.5 m for each case.

pneumatically operated clamp. The load cell transducer was connected to a data logger with a sampling rate of 50 kHz. The drop distance and grain mass were selected to utilize the linear region of the load cell transducer (Maranzano and Hancock 2016). A single grain with a diameter of 10 mm was loaded into the pneumatic clamp. The data-logger and camera were then initiated, after which the clamp was opened, allowing the grain to fall.

Numerical Modeling Procedure

The contact model adopted in this study is based on Hertzian contact theory [Figs. 3(a and b)]. A full description is given in Appendix I. The centroid of a single discrete element was generated a set distance (0.5 m) above a single horizontal plane. The horizontal plane modeled the load-measuring system (i.e., the combination of the load-bearing plate and the load transducer). The set drop distance corresponds to a preimpact velocity of around 3 m/s, characteristic of the velocities in the subsequent physical flume experiments of channelized granular flow impact. The horizontal plane had a mass M and could move in the z -direction [Fig. 3(c)]. This plane was retained by a spring element that enabled the displacements characteristic of the physical load transducer. The force on the spring element was given by

$$F_{\text{spring}} = -k_p x_z - \gamma_p U_z \quad (3)$$

where k_p = spring element stiffness (accounting for both the load-bearing plate and load transducer); x_z = displacement in the z -direction; γ_p = damping constant for the load-measuring system; and U_z = velocity in the z -direction. Critical damping was used for the simulations [i.e., $\gamma_p = (4Mk_p)^{1/2}$, because ideal load cell transducers should not continue to oscillate continuously after impact; M is the mass of the load-measuring system]. The transmitted load in the DEM load-measuring system could be calculated from F_{spring} . For each simulation, the grain was allowed to fall under the influence of gravity. The simulation was stopped when the grain had rebounded from the plane and after the plane had reached its maximum displacement.

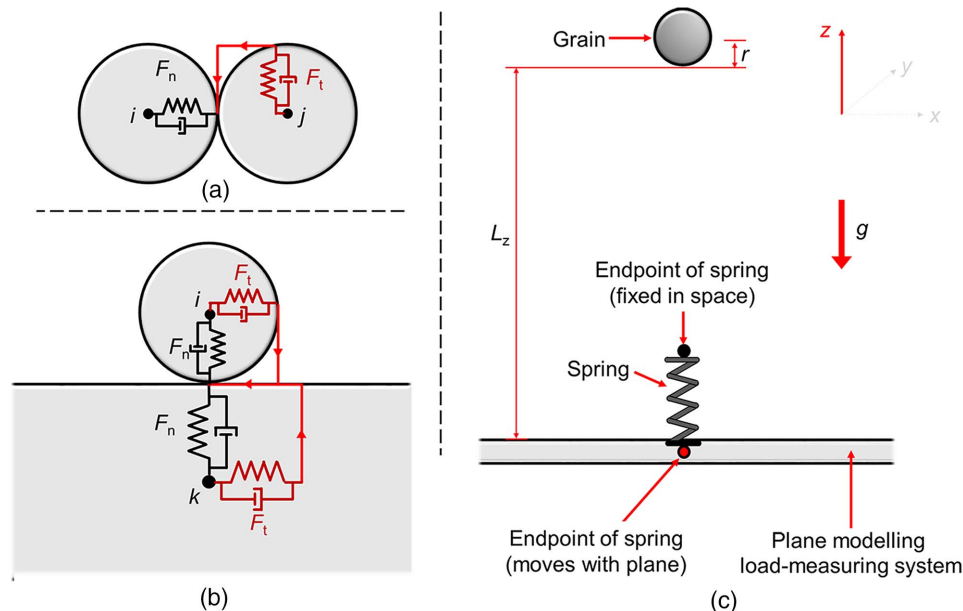


Fig. 3. (a) Side view schematic of the DEM contact model for grains; (b) side view schematic of the DEM contact model applied to the plane modeling the load-measuring system; and (c) side view schematic of the DEM setup for the drop tests, showing the spring element that models displacement of the load-measuring system in response to loading (including preloading due to gravity). Not drawn to scale.

Table 3. Test plan (drop tests)

	Test series	Load-measuring system: elastic modulus (GPa)	Mass ratio between load cell system and grain, M/m	Equivalent spring stiffness of load cell system, k_p (N/m)
Comparison	Physical drop tests	—	50,350	—
	DEM drop tests	200 (steel) 1 (acrylic)	50 350	2×10^9 2×10^9
Parametric	DEM drop tests	50 (glass/aluminum)	$0.1 < M/m < 1,000$	$10^5 < k_p < 10^{11}$

Physical Test and Numerical Simulation Plan

In the drop tests, a single grain diameter (10 mm) was adopted. The ratio between the mass of the plate and the grain, as well as the spring element stiffness, were varied. The grain and material elastic moduli were set to 50 GPa, which is characteristic of glass. Table 3 presents the test program for both the numerical drop tests and the physical tests.

Interpretation of Results: Single-Grain Drop Tests

Physical Measurements of Contact Force on Grain Impacting Load-Measuring System

Fig. 4 compares the physically measured impact load for two cases: with just the load transducer [Fig. 4(a)]; and with a single acrylic plate attached to the load transducer [Fig. 4(b)]. Bolts were used to attach the load transducer and plate together. The mass ratio M/m (where M is the mass of the load-cell system and m is the mass of the grain) was set at two values: 50 and 350. The inserts show data from the DEM using a critically damped spring element. The postimpact oscillatory behavior can be obtained by applying underdamping.

Critical damping was used for the simulations [i.e., $\gamma_p = (4Mk_p)^{1/2}$, where M is the mass of the load-measuring system]. Critical damping was adopted because it is ideal for load-measurement systems designed for dynamic impacts from granular flows, where many impacts take place over a short period of time. Overdamped load cells may not register the entire load for quick impacts, where the impact time is faster than the time required for the load cell to reach maximum displacement. In contrast, underdamped load cells make it difficult to differentiate between

successive impacts and postimpact oscillations. Both issues are highly relevant for load cells designed to capture loads from granular flows.

In practice, load cell transducers do not always include specifically designed damping mechanisms. Furthermore, attaching extra objects to load cell transducers modifies the mass and stiffness of the system, and hence the damping characteristics. Indeed, it is evident from the physical tests presented in Fig. 4 that there is a certain degree of underdamping, although the subsequent oscillations in Fig. 4(a) are less than 1/7 of the impact magnitude, indicating that the assumption of critical damping is not unreasonable. In any case, in this section, we are only interested in collisions from a single grain, so the behavior of the load cell after contact from the grain has ceased is not of primary importance. In other words, superposition of subsequent impacts with oscillations of the physical load-transducer system are outside the scope of this study, although they are relevant for physical studies on the impact of granular flows (e.g., Scheidl et al. 2013; Vagnon and Segalini 2016; Song et al. 2017, 2018). Underdamping can be captured in the DEM model by reducing the damping coefficient, as shown in the inset of Fig. 4(b).

With regard to the peak of the impact force, it is higher for Case a than for Case b. The period of oscillations after impact also increases from Case a to Case b. Both effects are due to the increased of the load-transducer system.

The DEM simulations shown in the inserts were run using material parameters corresponding to the physical experiments (Table 3). Initial peaks of a similar magnitude are observed for both Cases a and b, although it can be observed that in Case b, the computed DEM load is about twice that of the physical load. The fact that the difference is this large is surprising because physically meaningful parameters were, as far as possible, adopted for the

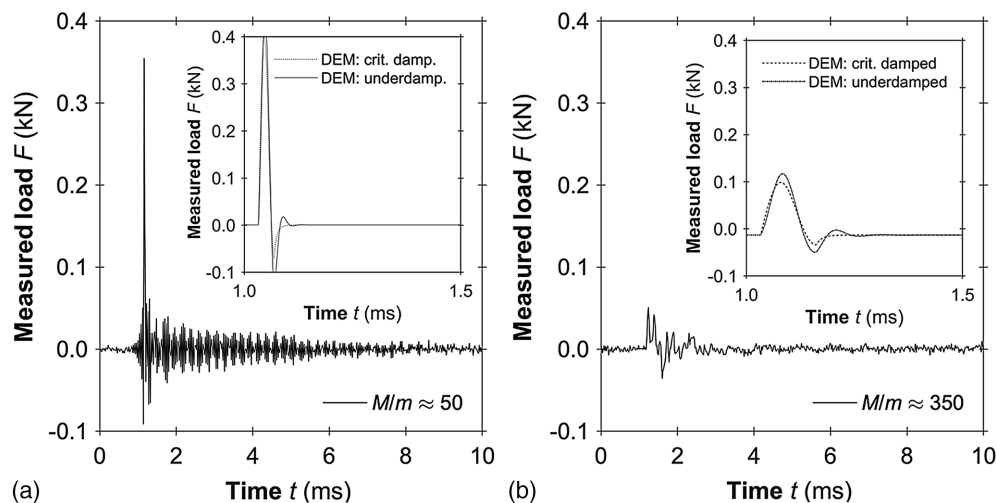


Fig. 4. Drop test results showing the physical load output by the load cell. The objects impacted are (a) the load cell itself; and (b) the load cell with a plate mounted on the load cell. The inserts show DEM back-analyses using material parameters for input, assuming that the load cell is critically damped. If the load cell is modeled as being underdamped, a similar force-time history can be modeled using the DEM.

DEM backanalyses. Nonetheless, comparison with physically measured loads is how some studies calibrate their DEM models (e.g., Cui et al. 2018; Leonardi et al. 2019). Furthermore, the disparity between physical and computed loads implies that DEM studies recommending loads for practical engineering may be overconservative if output is based on realistic input parameters.

The difference in the size of the physical and computed loads nonetheless suggests that other factors besides the increased mass of the load-transducer system (i.e., the mass of the load transducer plus the mass of the plate) contribute to a decrease in the impact force transmitted as load. Such factors may include, for instance, a reduced composite stiffness of the load-transducer system due to the plates having a finite bending stiffness. Trying to get around these limitations will necessarily include certain trade-offs. For instance, increasing the rigidity of a load-transducer system is likely to come with an increased mass. The benefits of the increase in the system rigidity on the ratio between impact force and load measured may be offset by the increase in the system mass, which tends to reduce transmitted load. Nonetheless, the scope of this study is restricted to addressing scaling effects due to (1) the mass of the load transducer system, and (2) the scale of the experimental model, and so a detailed investigation of other potential effects is deferred for future studies.

The equivalent spring stiffness of the load transducer k_p can be estimated based on the period T of each vibration for Case a, where no plate was attached to the load cell. It should be emphasized that only the initial peak is due to a collision from the dropped grain, which impacts the load cell only once; subsequent peaks occur due to continued oscillations of the load cell around the rest point. These oscillations can nonetheless be used to identify the natural period T by looking at the time required for a full cycle (i.e., neutral-peak-neutral-trough-neutral). It was hence found that the period for the load cell is about $40 \mu\text{s}$. Assuming that it oscillates at its natural frequency, k_p can be written as $M(2\pi f)^2$, where f is the frequency, and k_p can then be found to be around $2 \times 10^9 \text{ N/m}$.

Following a similar procedure, k_p for the case where $M/m = 350$ is around $1 \times 10^9 \text{ N/m}$. For single impacts, as long as the response time of the spring (governed by k_p) is shorter than the impact time, k_p should not affect the maximum load registered. The maximum load is instead governed by the material stiffness parameters (including the Young's modulus).

Computed Contact Force on Grain Impacting Load-Measuring System

In this section, the influence of the stiffness of the spring element, as well as the mass of the load-measurement system M relative to the grain mass m , are investigated. According to Kluger et al. (2016), the magnitude of the physical load that is to be measured dictates the spring element stiffness k_p that should be adopted. Generally speaking, load transducers that are rated for higher loads are stiffer. As for the effective mass ratio (e.g., Christoforou et al. 2013), high ratios of M/m can be classed as infinite structure problems, wherein the structure is much larger than the impacting grain. This condition is characteristic of experiments where granular flows impact an instrumented barrier plate (e.g., Caccamo et al. 2012; Song et al. 2017). Lower mass ratios (e.g., unity) may be adopted for impacts from individual bodies. Smaller ratios of M/m are also shown for completeness, although it is not expected that load-measuring systems much lighter than the impacting grains would be used (e.g., because of potential yielding).

Here, the quantities studied are (1) the maximum grain force (Appendix I gives the constitutive Hertzian soft-sphere equations),

and (2) the load measured by the load-transducer system implemented in the DEM ($F = k_p x_z$). The grain force should increase with the barrier rigidity. For design purposes, the highest force possible for a given collision-corresponding to an immobile barrier should be adopted to be conservative. The ratio between the aforementioned two quantities indicates how much of the force is transmitted as load.

Fig. 5(a) shows the maximum grain force obtained using the one-dimensional DEM formulation. The equivalent linear material stiffness of the grain k_g is shown for reference, and was calculated using the following relationship from Leonardi et al. (2014), ultimately derived from a Hertzian formulation:

$$k_g = \frac{8}{15} \cdot \frac{E_g}{1 - \nu_g^2} \sqrt{r_g^*} \quad (4)$$

where E_g = elastic modulus; ν_g = Poisson's ratio; r_g = radius; and the subscript g = grain. In practical terms, setting the spring element stiffness of the load-measurement system to a value higher than k_g implies that a load transducer will not measure any load. This is because the system response is always governed by the lowest stiffness. Nonetheless, the computed grain force from the Hertzian formulation should not be strongly affected.

For $M/m \geq 1,000$ (i.e., the barrier is at least 1,000 times more massive than a single grain), the grain force ceases to increase and can be considered an upper bound. The spring element stiffness k_p has a minimal effect because the mass of the barrier tends to prevent it from moving in response to impacts from the grain. This minimizes

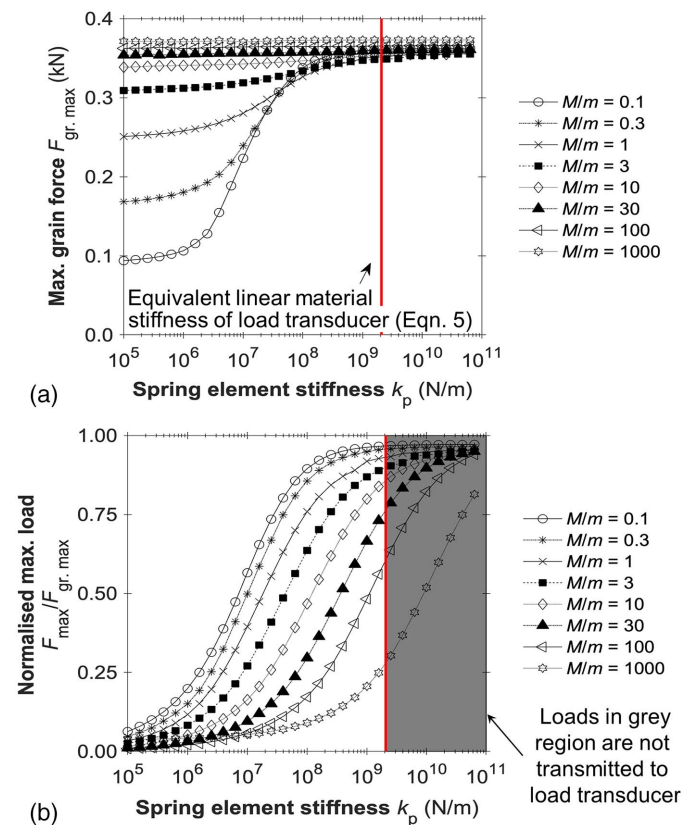


Fig. 5. Forces and loads involved in impacts between grains and barrier plate: (a) peak grain force, extracted from the DEM; and (b) the loads computed using the plane in the DEM, based on the maximum displacement and the spring stiffness following a collision from the grain, normalized by the theoretical maximum reaction force on the grain.

the impact time, which tends to maximize the impact force because $F \propto 1/\Delta t$ (e.g., Ashwood and Hungr 2016; Leonardi et al. 2016). In contrast, for $M/m = 0.1$ (where the grain is 10 times more massive than the barrier), the Hertzian grain force reduces to around less than 10% of the upper bound for $k_p = 10^5$ N/m. This is because the spring element undergoes a large displacement, lengthening the impact time and hence reducing the Hertzian grain force. The impact behavior is reminiscent of flexible barriers (e.g., Song 2016). For a larger spring element stiffness of $k_p = 10^9$ N/m, the grain force increases to around 90% of that for $M/m = 1,000$.

Fig. 5(a) indicates that as long as requirements for the composite stiffness required for a particular load are met (i.e., the barrier cannot flex too much when impacted), and if the load-transducer system is very light compared with the grain (i.e., the effective mass ratio M/m is low), Hertzian grain forces corresponding to an immobile barrier (i.e., a completely rigid barrier) can be obtained.

Fig. 5(b) shows the transmitted load (obtained from displacement of the load-transducer system; F_{spring}) divided by the maximum grain force for a perfectly immobile barrier [Fig. 5(a)]. This ratio indicates how well the load-transducer system measures the transmitted load. If the stiffness of the moving components within the load cell are higher than the material elastic modulus E , then the material properties of the load cell will govern and no load can be measured. For a mass ratio $M/m = 0.1$ and a spring element stiffness of $k_p = 10^5$ N/m, the normalized load is around 10%, indicating poor load transmission. The normalized load for this mass ratio climbs to around 90% for $k_p = 10^8$ N/m, indicating high load transmission. At the other extreme, for $M/m = 1,000$ and $k_p = 10^5$ N/m, the normalized transmitted load is almost zero. The normalized transmitted load climbs to just 20% for $k_p = 10^9$ N/m, near the upper limit for the maximum acceptable spring element stiffness.

The inability of more massive load-measuring systems to measure loads is because of their mass, which tends to resist translational movement. The impulse from the grain is too short for the barrier to reach the maximum displacement required to measure the full load, according to $F = k_p x_z$. This phenomenon can be quantified using a simple ratio of timescales for (1) the vibration of the load-measuring system, and (2) the contact between the grain and the upstream face of the load-measuring system. The timescale for a full cycle of vibration for a barrier plate t_p —assuming it vibrates at its natural frequency—can be written as follows:

$$t_p = 2\pi\sqrt{\frac{M}{k_p}} \quad (5)$$

An expression for the time scale for the contact time of the grain was proposed by Leonardi et al. (2014), modified from a similar formulation from Antypov and Elliott (2011) based on a Hertzian formulation, and is given

$$t_g = 2.5\left(\frac{m^*2}{k_g^2 U_1}\right)^{0.2} \quad (6)$$

where m^* = weighted mass ratio; k_g is calculated from Eq. (4); and U_1 = preimpact velocity. A dimensionless number that roughly indicates the proportion of load likely to be measured by the load transducer can then be written

$$\Gamma = \frac{t_g}{t_p} \quad (7)$$

For $\Gamma > 1$ (i.e., $t_g > t_p$), the load-measuring system should be able to reach its maximum displacement x_z . Conversely, for $\Gamma < 1$

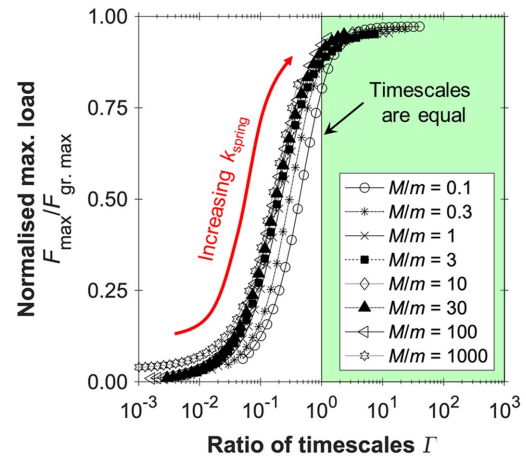


Fig. 6. Peak load computed using the plane in the DEM normalized by the peak grain force as a function of Γ .

(i.e., $t_g < t_p$), the composite force from the load-measuring system will tend to push the plate back toward the neutral point as soon as the force from the impacting grain stops being exerted. As such, the maximum displacement is not reached, and the force is not completely transmitted as load.

Fig. 6 shows the dimensionless number Γ for various spring element stiffnesses and mass ratios. Values of $\Gamma > 1$ appear in the shaded region. Values of $\Gamma > 1$ correspond to normalized load $F_{max}/F_{grain max}$ of 0.9 or above. As expected, lighter barriers (i.e., lower values of M/m) are associated with higher values of Γ for a given spring element stiffness k_p . Eq. (7) appears to be able to provide a reasonable estimate for the ability of a load-measuring system to capture forces from impacting grains, at least within a Hertzian framework.

A few extra points are worth mentioning here. Firstly, the load transducer system should be as light as possible, although rigidity is clearly another concern. The spring element stiffness k_p (which is a function of the capacity of the load transducer) should be selected according to the loads expected while minimizing the displacement (e.g., Kluger et al. 2016; Maranzano and Hancock 2016).

Secondly, for static loading, the time scale for contact between grains and the barrier tends to infinity [Eq. (7)], so for this limit neither the spring element stiffness nor the mass of the load-transducer system affect the loads output for a given Hertzian force (Christoforou et al. 2013).

Thirdly, for studies on granular flows impacting a barrier (e.g., Ishikawa et al. 2010; Canelli et al. 2012; Jiang and Towhata 2013), the equivalent mass ratio (M/m) is likely to fall in the range $M/m \gg 10$ (although it is unfortunately not possible to back-calculate exact values based on the information given in such papers) (Table 1). For the physical instrumented barrier used for the subsequent channelized granular flow tests shown in Fig. 7(b), the mass of each acrylic plate is 212 g, and the mass of the load transducer itself is 74 g. The mass of each of the 10-mm grains is $(4/3 \times \pi \times 0.005^3) \text{ m}^3 \times 2,650 \text{ kg/m}^3 = 1.4 \text{ g}$. This gives a ratio M/m of about 200, so Fig. 7(b) implies that it is not possible to measure the full dynamic load from discrete impacts at the flow front using this configuration. The extent of the undermeasurement can nonetheless be estimated from graphs such as Fig. 5(b) or 6 by calculating the equivalent mass and equivalent material linear stiffness ratios. Furthermore, this undermeasurement should be recognized by researchers using such data to calibrate numerical models (e.g., Cui et al. 2018; Leonardi et al. 2019) because the

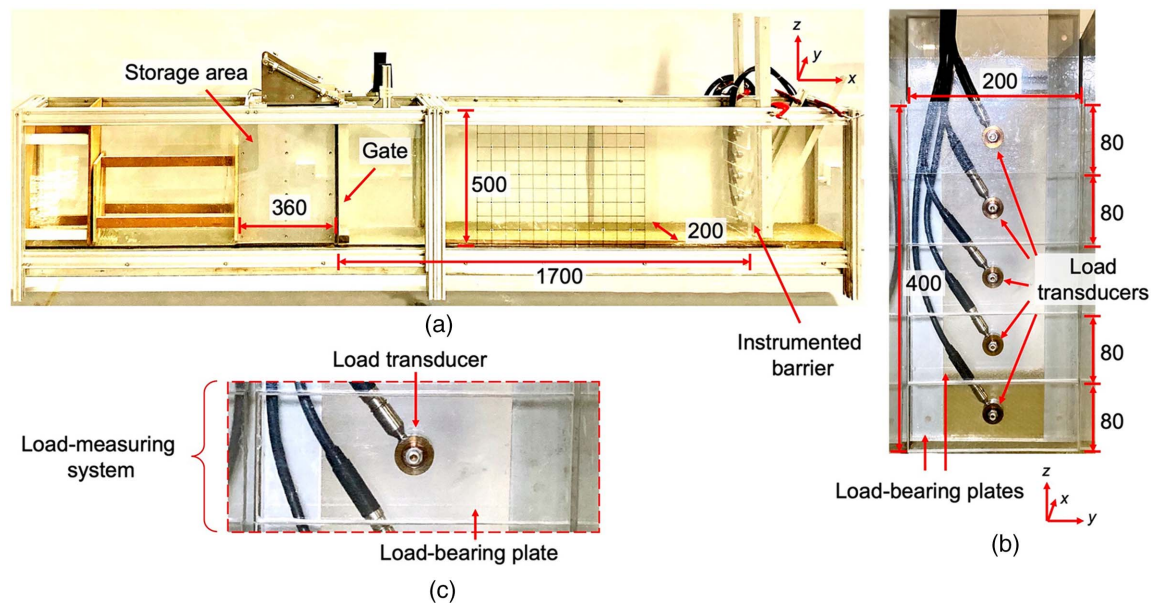


Fig. 7. Physical setup for granular flow impact tests: (a) side view of flume; (b) front view of instrumented barrier; and (c) individual view of one load-measuring system. All dimensions in millimeters.

loads measured may not be representative of the actual forces involved.

Methodology: Channelized Granular Flows

Physical Flume Tests

Physical flume tests were performed as a benchmark for the DEM simulations. The flume was 0.2 m wide by 0.5 m deep, and had a length of 3.0 m (Fig. 7). A high-speed camera (Prosilica GE640, Allied Vision Technologies GmbH, Stadroda, Germany) with a frame-rate of 300 frames per second (FPS) and a resolution of $1,500 \times 1,000$ pixels faced the sidewall to capture the flow kinematics. A total mass of 40 kg of uniform glass spheres with individual diameters of around 10 mm was placed into a storage section at one end of the flume. The mass of each sphere was 1.4 g, with a material density of around $2,650 \text{ kg/m}^3$.

An instrumented barrier with five load transducers attached to individual load-bearing plates made of acrylic was placed at the other end of the flume. The load-bearing plates were attached using screws integrated into the load transducers. The mass of each plate was 212 g, and the mass of the load transducers was 74 g. A pneumatically operated gate was used to retain the grains before dam-break. After inclining the flume to the desired inclination and starting the camera, the gate was opened.

Numerical Modeling: Channelized Granular Flows

The open-source DEM model LAMMPS Improved for General Granular and Granular Heat Transfer Simulations (LIGGGHTS) (Kloss and Goniva 2010), was used to perform granular flow impact simulations. A total mass of 40 kg of discrete elements (Choi et al. 2016; Goodwin and Choi 2020) was generated randomly within a storage area at the head of the channel. The size of the grains was $10 \pm 1 \text{ mm}$, following an approximately Gaussian distribution. Applying a slight degree of polydispersity is one way of minimizing artificial crystalline structures from appearing (e.g., Marchelli et al. 2019). After the grains had settled within the storage area, the direction of gravity was changed to simulate

inclining the channel. The grains were again allowed to come to rest. Thereafter, the gate (modeled as a plane separating the storage area and the channel) was deleted, enabling dam-break conditions (Iverson et al. 2010; Ashwood and Hungr 2016). The grains were thus allowed to move downstream and collide with the barrier.

It should be emphasized that the barrier was not modeled in the same way for the simulations with a single discrete element and for simulations of channelized granular flows. The simulations with a single discrete element were used to assess the effects of the mass of the load cell system on the load measured. As such, the modeled barrier had a particular mass and equivalent spring stiffness.

For the DEM simulations of granular flows, the barrier was modeled instead as an immobile plane with no mass. This is the way in which all DEM studies on flow-barrier interaction that we reviewed modeled the barrier (specifically, An and Tannar 2007; Teufelsbauer et al. 2009; Salciarini et al. 2010; Teufelsbauer et al. 2011; Shan and Zhao 2014; Albaba et al. 2015, 2018; Law et al. 2015; Ng et al. 2017; Shen et al. 2018; Cui et al. 2018; Marchelli et al. 2019) (Table 2). The effects of barrier vibration on measured impact loads for granular flows are discernible a priori, in that superposition occurs. The influence of this superposition on measured loads is evaluable through single-grain drop tests, measuring the maximum negative load registered by the load transducer. Given these considerations, it was chosen to model the barrier plate as though it was rigid for the channelized granular flow tests. This choice is especially helpful for evaluating results from the other DEM studies on granular impact.

The barrier interacted with the discrete elements using the Hertzian contact model. Stiffness parameters and the coefficient of restitution were defined to be the same as that of the discrete elements. Making the stiffness coefficients unequal has a predictable effect on the measured loads, as shown by Eq. (19) in Appendix I: reducing either one leads to a reduction in the composite Young's modulus, and a corresponding decrease in the computed impact loads. Furthermore, the coefficient of interface friction on the barrier was the same as the other boundaries in the model.

Selection of DEM Parameters for Channelized Flow Simulations

According to Coetzee (2017), there are two main ways of calibrating DEM models: either by measuring properties at the grain level, or by observing the bulk behavior of a physical array of grains and iteratively changing numerical parameters until the DEM model is able to reproduce the behavior. Indeed, the process of validating DEM parameters for granular flows through comparison with physical flow kinematics is well-established (e.g., Teufelsbauer et al. 2009, 2011; Shen et al. 2018; Marchelli et al. 2019; Zhang and Huang 2021). Coetzee (2017) nonetheless noted that there are no standardized techniques for either type of calibration. In this study, we use values derived from a combination of the two techniques: the interface friction angle was directly measured, whereas the internal friction angle was calibrated iteratively.

The interface friction angle came from direct measurements from a tilt-test by Choi et al. (2016), following the procedure outlined by Pudasaini et al. (2007), Mancarella and Hungr (2010), and Jiang and Towhata (2013). Specifically, a cylindrical container with a diameter of approximately 20 cm, open at both ends, was filled to a depth of around 10 cm with glass beads. The container was placed on a filmed acrylic board. The board was then gradually inclined until the cylinder started to move, at which point the inclination of the board was recorded. This procedure was repeated several times to characterize the error. A further evaluation of the friction parameters through a comparison of physical and computed flow kinematics is also provided in this study, in Fig. 11.

The internal friction angle was set at 19.8° , which was back-calculated by comparing the flow and impact dynamics of physical and numerical flows from Ng et al. (2019) following the iterative procedure related by Coetzee (2017). Ng et al. (2019) conducted physical flume tests using an open-channel flume identical with the one in this study, and 40 kg of glass spheres with a diameter of 10 mm were used. DEM back-analyses of these tests, which were geometrically identical with the physical tests, were then performed to compare the flow depths and flow velocities for a range of friction angles. The value of 19.8° was found to give the best match with the physical flow kinematics. This back-analyzed friction angle was subsequently also adopted by Goodwin and Choi (2020) and Goodwin et al. (2021), who both used the DEM to model granular flows. Both studies also included separate calibrations against physical flow experiments with different boundary conditions. The varied boundary conditions included both open and closed barriers in the channel, as well as roughened basal boundary conditions; reasonable matches were obtained between physical and DEM results for each case. In the latter study, physical and numerical output for the pileup height and outflow rate of spheres impacting an open barrier (i.e., a barrier with a vertical slit) were compared in addition to the flow kinematics across a range of channel inclinations, and a close quantitative match was found.

The effects of the friction parameters on the flow dynamics are mediated entirely through tangential forces, which are also functions of the coefficient of restitution and the mass of the grains (Appendix I). Indeed, the coefficient of restitution depends on both colliding objects, as well as their relative masses. Ng et al. (2019), used physical drop tests similar to those in this study to characterize the coefficient of restitution of glass beads with a diameter of 10 mm. When impacting a fixed steel slab, the coefficient of restitution was 0.74. Chau et al. (1998) found a coefficient of restitution in the range 0.39–0.49 for rock fragments falling onto slopes. Hungr and Evans (1988) back-analyzed a coefficient of restitution of 0.5 for rockfalls. The DEM studies collected in Table 1 adopt

values of between 0.2 and 0.8. In this study, we select 0.5 as a maximum plausible value of the coefficient of restitution that might be relevant to cases in the field, given our interest in scale effects.

Scaling for Flume Tests

We introduced a dimensionless geometric scaling factor Ω for the latter part of this study. For the DEM simulations of channelized flows, all distances were varied by Ω , including the channel width B , grain diameter δ , and distance from the gate to the barrier L . Ω gives length scales relative to the laboratory-scale flume used for the physical tests in this study. Parameters such as the elastic modulus E and the material density ρ were not varied because they are material constants. Indeed, E has been shown to have very limited influence on open-channel flow dynamics for dry granular flows (e.g., Kumaran and Bharathraj 2013; Kneib et al. 2016, 2017, 2019). The bulk density was found to vary almost negligibly with scale, consistent with Iverson (2015), who stated that this should be the case for flows that are dry and nearly or completely monodisperse. An example of the DEM models at different scales Ω is shown in Fig. 8.

As for ensuring dimensional similitude, to characterize the flows, dimensionless scaling numbers can be used to compare the dynamics of the flows in this study relative to field events. The Froude number Fr gives the ratio of inertial forces to dynamic forces (Armanini et al. 2011, 2014; Armanini 2015; Choi et al. 2015; Ng et al. 2016, 2019)

$$Fr = \frac{U}{\sqrt{gh \cos \theta}} \quad (8)$$

where U = velocity; g = gravitational acceleration; h = flow depth; and θ = channel inclination. Fr for channelized granular flows in the field can vary depending on the flow type, but they lie within the range $0 < Fr < 7.5$ for debris flows (Hübl et al. 2009), which may have coarse granular fronts. The procedure for characterizing Fr reported by Ng et al. (2019), i.e., characterizing Fr using a static monitoring region for open-channel DEM flows, was adopted.

Fig. 9 shows Fr for open-channel flows at six channel inclinations ($10^\circ < \theta < 30^\circ$) as a function of time along the length of the flow. Time $t = 0$ s was set when the front of the flow started to enter the monitoring region. The monitoring zone was 100 mm long and was centered 1.7 m downstream, where the barrier would have been. The minimal Fr for each flow was within the reported range for prototype debris flows (Hübl et al. 2009).

Froude numbers Fr for open-channel flows at different scales, denoted by a dimensionless geometric scaling factor Ω .

Fig. 10 shows open-channel flows similar to those in Fig. 9. In Fig. 10, the channel inclination θ is 30° for each case. The scale factor Ω was varied from 0.25 to 128 (Fig. 8 gives a graphical definition of Ω). The abscissa is normalized by $\sqrt{\Omega}$ to scale time to the laboratory scale flume experiments. Figs. 10(a–d) were sampled at points relative to the position of where the downstream barrier would be in the subsequent simulations of granular flow impact (i.e., $L = 1.7\Omega$ m). Specifically, Figs. 10(a–d) correspond to $0.25L$, $0.5L$, $0.75L$, and L . The normalized time starts when the flow enters the first monitoring section. Lines show the entire set of extracted data, and markers are plotted every n values for clarity. The collapse in data when plotted against normalized time occurs regardless of where the static monitoring section is placed, indicating similitude of Fr along the length of the channel.

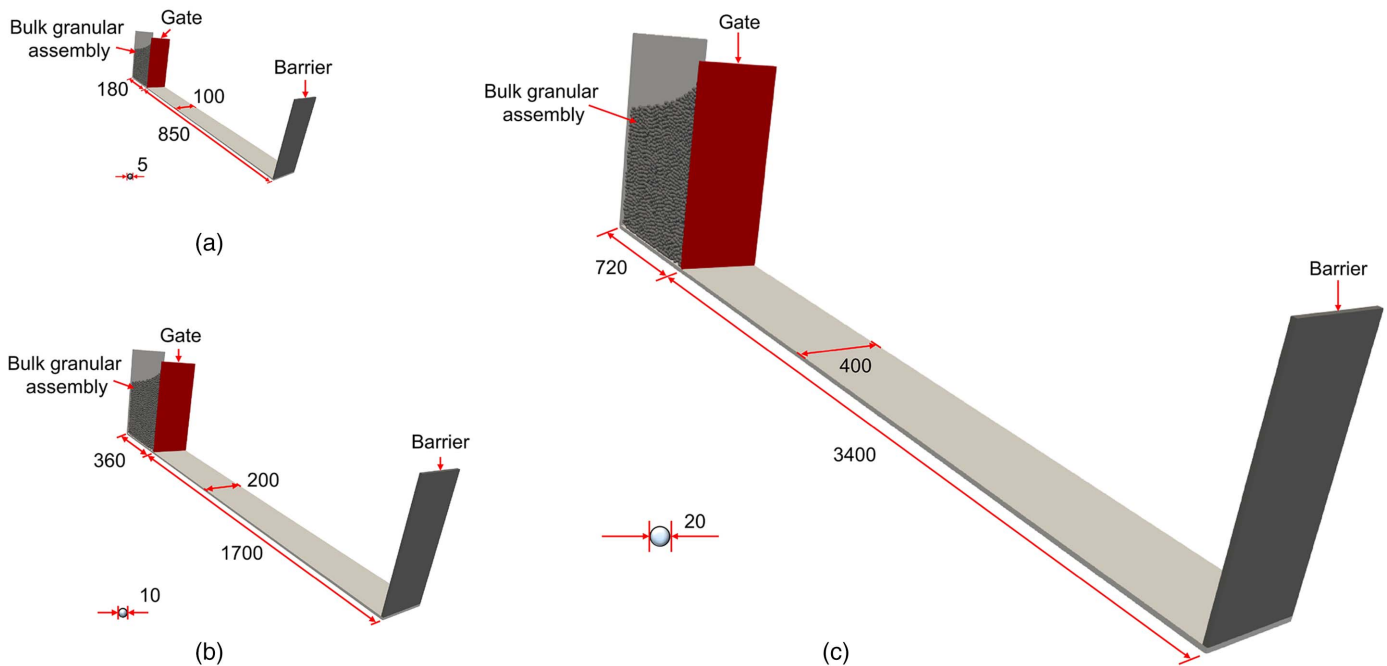


Fig. 8. DEM setup for granular flow impact tests for different scale factors Ω : (a) $\Omega = 0.5$ and $\delta = 5$ mm; (b) $\Omega = 1.0$ and $\delta = 10$ mm; and (c) $\Omega = 2.0$ and $\delta = 20$ mm.

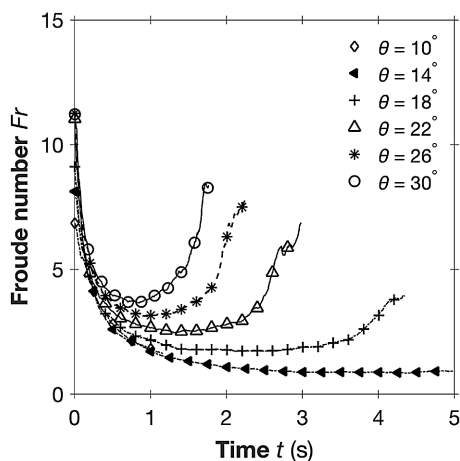


Fig. 9. Froude numbers for open-channel flows passing a point $L = 1.7$ m downstream, varying the channel inclination θ . Lines show the entire set of extracted data, and markers are plotted every n values for clarity.

Physical Test and Numerical Simulation Plan Program

Both physical experiments and DEM simulations of flows impacting a barrier were performed at inclinations of between 10° and 30° , with an immobile plane placed orthogonally to the channel base 1.7 m downstream from the storage area. The placement of the barrier was chosen with due consideration to the Froude numbers of the flows (Figs. 9 and 10). In the first set of DEM simulations, both the elastic modulus E and channel inclination θ were varied. In the second set of simulations, the geometric scaling factor Ω and elastic modulus E were varied. The plan for the physical flow tests and numerical simulations is presented in Table 4.

Interpretation of Results: Channelized Granular Flows

Comparison of Flow Dynamics

It was shown in previous sections that load-measurement systems used in granular flow experiments are likely to lead to discrete grain impact forces being incompletely transmitted as loads. This is ultimately because of the mass of the plates that are required to provide an interface with the flows to allow load transmission to the load transducer. In this section, we evaluate potential incomplete load transmission using both physical experiments and a DEM model. In the DEM simulations, the barrier is modeled as being immobile, as per other DEM studies on impact, which gives an upper bound for the load.

Fig. 11 shows physical and computed flows for 10° and 30° . Particle imaging velocimetry (PIV) vectors are overlaid to show the velocity fields (Thielicke and Stamhuis 2014). The longest vectors correspond to a velocity of about 4 m/s, and the other vectors are scaled in length accordingly. For both channel inclinations, the granular flow front approaches the slit-structure as a wedge [Figs. 11(a and e) and 11(b and e)], as reported in multiple other studies on granular flows (e.g., Gray et al. 2003; Hákonadóttir et al. 2003a; Choi et al. 2016; Ng et al. 2017, 2019). Runup then occurs [Figs. 11(a and f) and 11(b and f)] (Choi et al. 2015), although the runup height for the 10° case is minimal. As the flow material continues to advance downstream, the pileup height develops further [Figs. 11(c–f)] (Hákonadóttir et al. 2003b; Jóhannesson et al. 2009).

Figs. 11(c and d) show the computed kinematics observed using the DEM model. Both the shape of the flow as it impacts the barrier and the velocity field are broadly captured using the DEM model, suggesting that the full 3D model is able to capture the general kinematics of the flow. Changing the grain elastic modulus E does not change the bulk flow or impact kinematics, even for relatively low

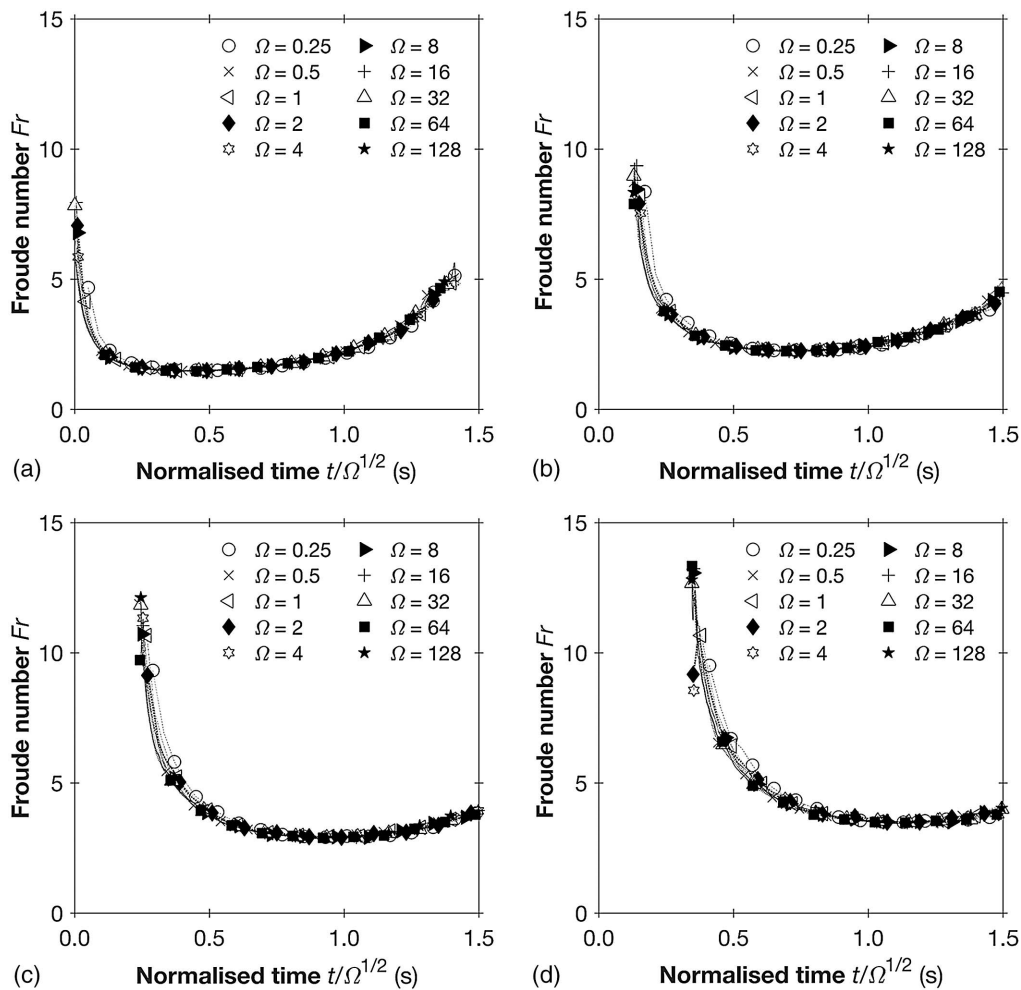


Fig. 10. Froude numbers Fr for open-channel flows at different scales, denoted by a dimensionless geometric scaling factor Ω .

Table 4. Test plan (channelized flow tests)

Test series	Grain elastic modulus (GPa)	Channel inclination, θ (degrees)	Scale factor, Ω
Physical flume tests	—	10, 14, 18, 22, 26, 30	—
DEM simulations: Fr	0.01, 0.1, 1, 10		1
DEM simulations: scale	0.01, 10	30	0.25, 0.5, 1, 2, 4, 8, 16, 32, 64, 128

values (e.g., [Kumaran and Bharathraj 2013](#)). Nonetheless, the computed impact load does change, as shown in the following section.

It should be emphasized that the number of particles in the physical experiments and the DEM simulations are the same; both have around 30,000 grains. This notwithstanding, for the tests at a channel inclination of 10° , the flow depth upstream of the barrier appears to be slightly higher for the DEM at around three grain diameters, whereas for the physical experiment, it is around two particle diameters. The degrees of concavity are also different, with positive concavity in the physical test and a more uniform layer for the DEM back-analysis. The reason for the varying degrees of concavity may be related to the assumptions of unchanging values of parameters in the flow, including friction coefficients and coefficients of restitution. Indeed, both the friction coefficients and the coefficient of restitution are recognized to vary with velocity and stresses (e.g., [Jop et al. 2006](#); [Lam et al. 2018b](#); [Sandeep et al. 2020](#)). For flows at different inclinations, the stresses and

velocities within the flow must change, so deficiencies in the set of DEM parameters originally determined from comparisons of physical and numerical flows at higher inclinations [22° to 30° ([Ng et al. 2019](#); [Goodwin and Choi 2020](#); [Goodwin et al. 2021](#))] may lead to differences in observed kinematics at lower inclinations.

As the impact process is beginning, loading is predominantly at the base of the plate. The translational movement of the load cell system that is required for measuring loads can be accompanied by rotational movement, especially during this initial part of the impact process. It is thus prudent to assess if rotational movement is likely to be important.

The moment at the tip of a cantilever beam, can be calculated as follows:

$$\delta_{\text{moment}} = \frac{(FL_{\text{beam}})L_{\text{beam}}^2}{2EI} \quad (9)$$

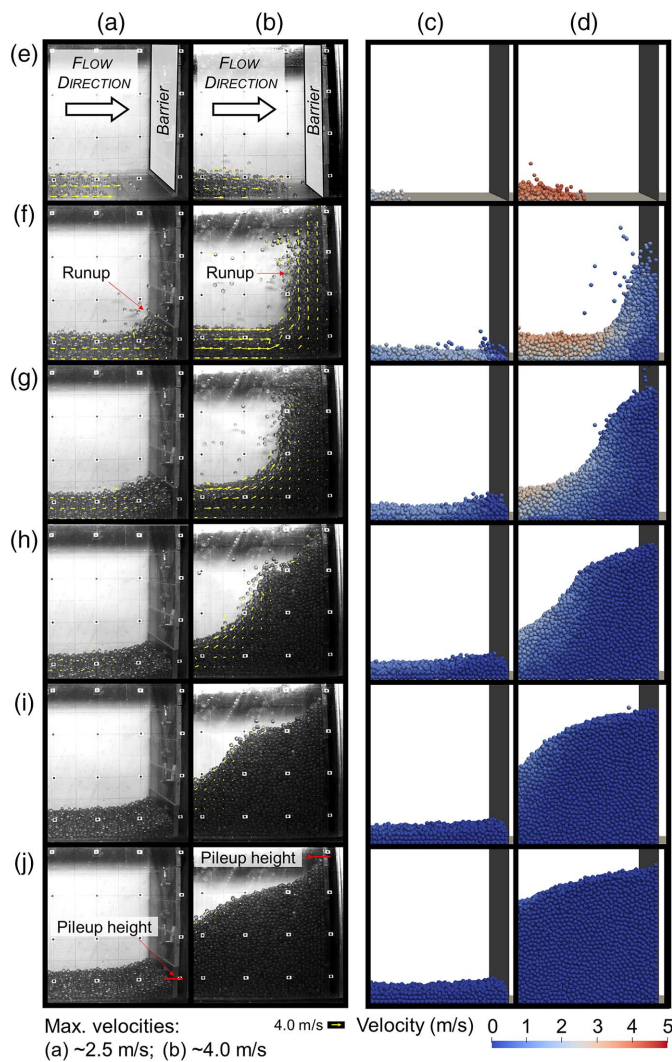


Fig. 11. Comparisons of physically observed flow kinematics with PIV vectors against computed DEM flow kinematics: (a) physical 10°; (b) physical 30°; (c) DEM 10°; (d) DEM 30°; (e) $t = 0.0$ s; (f) $t = 0.2$ s; (g) $t = 0.4$ s; (h) $t = 0.6$ s; (i) $t = 0.8$ s; and (j) $t = 1.0$ s.

where F = impact load; E = elastic modulus; L_{beam} = length of the beam; and I = second moment of area given by $I = DL_{\text{beam}}^3/3$, where D is the thickness of the plate. For the impact load of 0.3 kN measured in the drop tests, and assuming an elastic modulus of 300 GPa for the plates of the measuring system, this corresponds to a maximum deflection of about 2.4% that of the distance between the edge of the measuring system plate and the load cell.

This calculation implies that the rotation of the plate of the load-measuring system is insufficient to affect the translational ability of the load transducer: the translational load transmission should only be slightly affected. Steps to reduce the rotation of the system—for instance, increasing either E or I —are constrained by the increase in mass (and hence translational inertia) caused by increasing the rigidity.

Indeed, it would appear that the most favorable solution is instead reducing L , the distance between the edge of the plate of the load-measuring system and the load transducer, by installing load cells as close together vertically as possible [similar to the load cell transducer array of Scheidl et al. (2013)].

Comparison of Impact Dynamics: Physical and DEM

Fig. 12 shows the impact load time histories on a barrier for three cases: (1) physical load measurements obtained by summing the contributions from each of the five load transducers [Fig. 7(b)]; (2) loading on the barrier for $E = 0.01$ GPa using the DEM; and (3) loading on the barrier for $E = 10$ GPa, also using the DEM. These values cover typical values of E input into the DEM, within the limits of the program adopted (LIGGGHTS) and the requirement for high-frequency sampling of contact forces. $E = 10$ GPa approaches the elastic modulus of geological materials. Values of E are applied to both the bulk granular assembly and the barrier; the effective elastic modulus E^* is thus exactly $0.5E$ for each case.

Six channel inclinations are shown covering a range of Fr appropriate to prototype geophysical hazards (Fig. 9) (Hübl et al. 2009). The final static load is about the same for all three cases, which lends further confidence to the input parameters used for the model and also shows that the elastic modulus has a minimal effect on the flow dynamics. Furthermore, reference lines are plotted in Figs. 12(b and c) corresponding to the theoretical impact load using the Hertz equation with an analytic expression for overlap/deformation [Eqs. (1) and (2)] (Johnson 1985; Zhang et al. 1996). It was assumed that a single grain was dropped for the same vertical distance caused by inclining the channel (i.e., without considering losses due to bouncing, shearing, or rotation during outflow). These lines can be assumed to be interpreted as an upper bound for the impact load.

The relatively smooth increase of the physical loads [Fig. 12(a)] is because of the translational inertial effect of the barrier, which means that transient loads due to individual grain impacts are not captured. For each channel inclination, the load rises until the static load is reached. For these cases, the static loading appears to be sufficient for characterizing the maximum load.

The data from the physical load measurements [Fig. 12(a)] are closer to the DEM output for $E = 0.01$ GPa [Fig. 12(b)]. The DEM [Fig. 12(b)] does show a few transient loads due to the impact from individual grains, although none of these are greater in magnitude than the final static load. In contrast, for $E = 10$ GPa [Fig. 12(c)], there are large transient loads even for the lowest Froude number [Figs. 12(c and d)]. These are due to the frontmost grains, which impact directly on the barrier. The systematic overestimate of the load calculated using the Hertz equation [Eqs. (1) and (2)] occurs because it is assumed that the grain does not lose any energy as it moves downstream.

Load-Reduction Factor for Physically Measured Loads from Granular Flows

Fig. 12 has shown that impact loading behavior for a coarse granular flow impacting a barrier is governed by either (1) discrete Hertzian impulses, or (2) the final static load. For all of the physical tests performed, the static load appears to dominate. This is because the mass of each of the load-bearing plates tends to lead to incomplete transmission of grain force to measured load. Indeed, the DEM with an elastic modulus closer to that of typical geomaterials suggests that discrete loads from the dispersed front of the granular flow can govern the peak impact loading behavior instead of the final static load F_{static} .

Fig. 13 summarizes the maximum loads normalized by the final static load for a range of elastic moduli and channel inclinations modeled using the DEM. It should be reiterated that θ is a proxy for the Fr profile down a channel for a particular flow, as shown in Fig. 9. Higher values of θ are correlated with higher values of Fr . Reference lines based on existing analytic expressions are also plotted. The final pileup height at the barrier h_2 is calculated using an

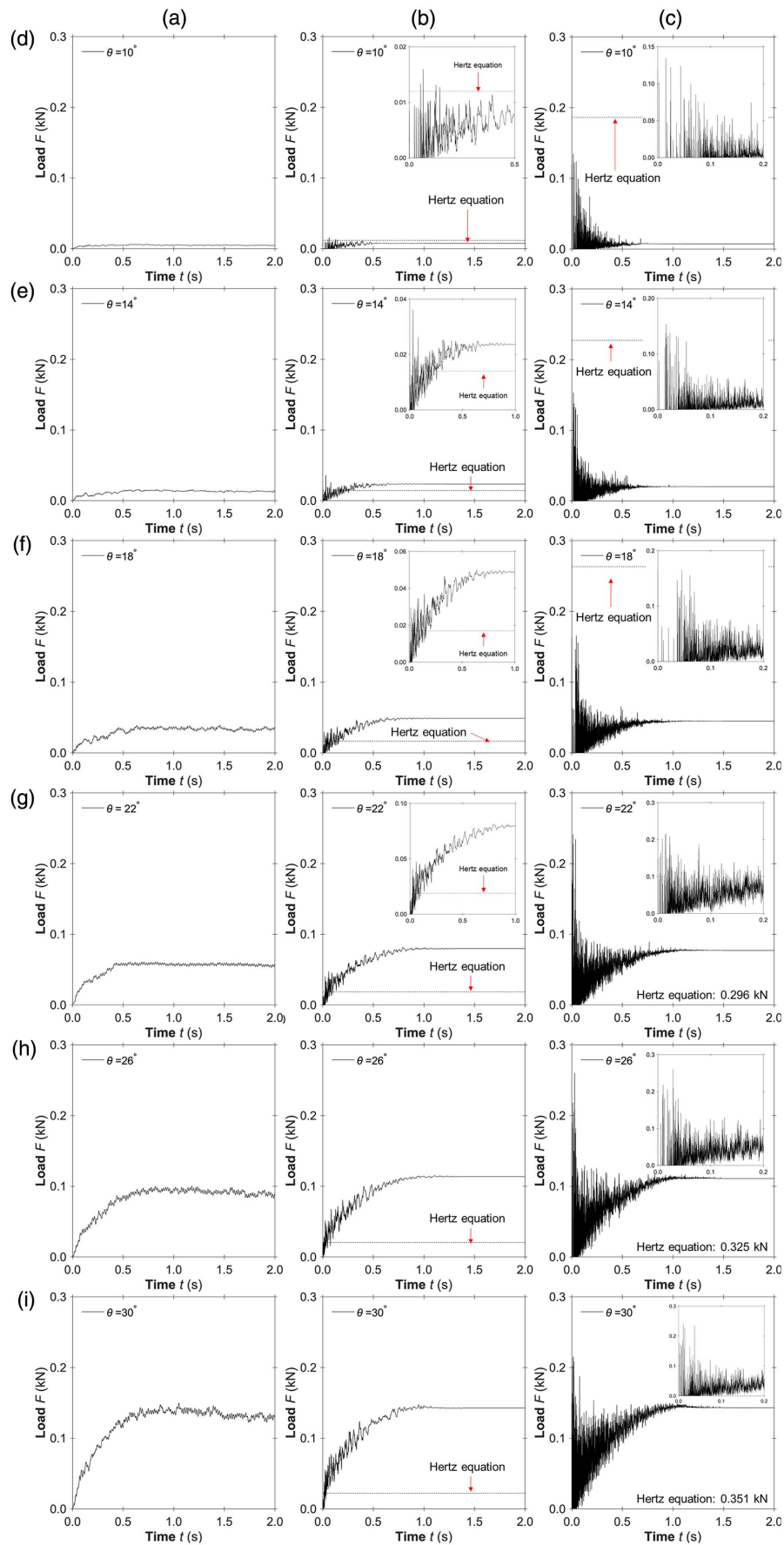


Fig. 12. Comparison of physically measured and computed impact load on barrier: (a) physically measured loads on the barrier; (b) computed loads from the DEM model for $E = 0.01$ GPa; (c) computed loads from the DEM model for $E = 10$ GPa; and six different inclinations: (d) $\theta = 10^\circ$; (e) $\theta = 14^\circ$; (f) $\theta = 18^\circ$; (g) $\theta = 22^\circ$; (h) $\theta = 26^\circ$; and (i) $\theta = 30^\circ$.

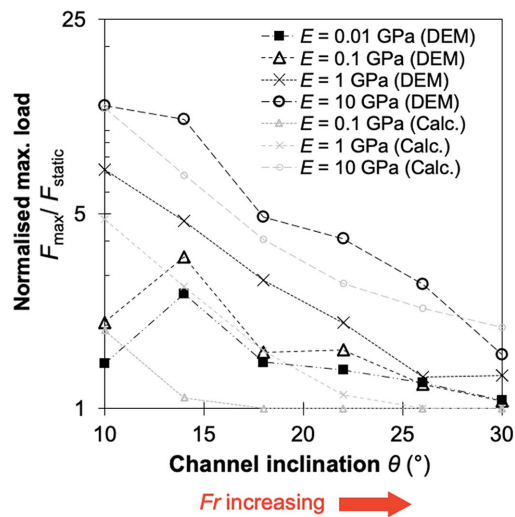


Fig. 13. Summary of ratio of maximum and final static loads computed from the DEM for the same series of elastic moduli shown in the previous figure. The reference lines are calculated from equations given by Hákonadóttir et al. (2003a) and Zhang et al. (1996) for Fr and h_1 relevant to flows at each channel inclination θ . Appendix II gives the system of equations.

analytic expression proposed by Hákonadóttir et al. (2003b) for a continuum flow impacting an immobile barrier, assuming an incompressible flow:

$$\frac{U_1^2}{gh_1 \cos \theta} + 1 = \left(\frac{h_2}{h_1}\right)^2 - \frac{h_2}{h_1} + \left(\frac{h_2}{h_1}\right)^{-1} \quad (10)$$

The first term is Fr^2 for an inclined channel; and h_1 = flow depth before impact. Values for each are taken from the longitudinal middle of the flow, where Fr is minimum and h_1 is maximum (Fig. 9). The value for h_2 can then be used to find the final static loading on the barrier

$$F_{\text{static}} = \frac{1}{2}(Bh_2 \cos \theta)(\rho \phi g h_2 \cos \theta) \quad (11)$$

where B = channel width; ρ = material density; and ϕ = solid volume fraction. As for the analytic Hertzian load, Eqs. (1) and (2) are adopted.

Fig. 13 shows that as the elastic modulus E is increased, the static load reduces in importance. Even for low channel inclinations and values for E much lower than those of typical geomaterials, the calculated Hertzian peak load can be double that of the static load.

Furthermore, there is a reduction of F/F_{static} as $Fr(\theta)$ increases. As Fr increases, the static load due to the pileup becomes relatively more important compared with the granular loading linked to the preimpact velocity [this can be shown using Eq. (10)]. Higher values observed for $E = 0.01$ GPa and 0.1 GPa at 14° occur because of concurrent impacts, which are more likely for softer materials due to longer contact times.

Collectively, this suggests that measurements from physical experiments tend to underestimate the load on the barrier. This is because of the relatively high mass of the barrier compared with impact from a single grain, and is a challenge for granular flow problems. Specifically, it is difficult to measure peak loads that correspond to the actual peak grain forces, as detailed in the section dealing with drop tests. As such, it is rather difficult to numerically model dynamic loads that match with physical measurements of

dynamic loading because the physical values of load do not correspond to full transmission of force. One solution to match these reduced loads that is common for DEM users (e.g., Law et al. 2015; Shen et al. 2018; Cui et al. 2018; Marchelli et al. 2019) is reducing the value of the elastic modulus E to unphysically low values. Low values of E mean that computational time can be reduced (e.g., Leonardi et al. 2014) with the flow dynamics relatively unaffected (Kumaran and Bharathraj 2013).

An alternative approach to using values of E that are physically correct but computationally expensive could be to use data such as that presented in Fig. 13 to assist in deconvolution of impact loads. It should nonetheless be noted that deconvolution of such signals involves other challenges, such as dealing with the changing composite translational inertia of the load-measurement system caused by the formation of the dead zone. However, such treatments are outside the scope of this study.

Loading Behavior at Different Scales

This study has so far looked at scaling issues caused by the impact of grains on barriers, both for single grains and for channelized flows. In this final section, the effects of the scale of the flow itself are preliminarily investigated using existing theory and the Hertzian DEM. As discussed previously, DEM simulations were run at different scales characterized using a dimensionless geometric scaling factor Ω (Fig. 8 offers a graphical depiction of Ω). Froude similarity for each of the cases at different scales has already been established (Fig. 10). In this section, the load on the load-measuring system (the barrier) is calculated directly from the overlap between the grains and the barrier and can thus also be referred to as the Hertzian grain force. This is different from earlier in the study where for single-grain collisions, the load was calculated by allowing the load-measuring system to displace elastically and then calculating the degree of displacement.

Time-histories from this investigation are shown in Fig. 14. The bulk normalized load is shown in black. The highest instantaneous load on an individual grain in contact with the barrier at each time step is also shown. The grain that is sampled can thus change between time steps. All loads shown are normalized by the final static load from the bulk granular assembly that was computed for each case. The horizontal gray line shows the final static loading, and is always unity due to the normalization adopted. Two representative values of both E and Ω are shown to highlight the changes in loading behavior for extreme cases. As the scaling factor Ω is increased from 1 to 128, the magnitude of the Hertzian impulses relative to the final static load tends to decrease. Furthermore, consistent with results shown in Figs. 12 and 13, the magnitude of Hertzian impulses increases with the elastic modulus E .

The reason for the scaling factor affecting the ratio F/F_{static} can be shown theoretically [discussed in Appendix II, which manipulates equations from Johnson (1985), Zhang et al. (1996), and Hákonadóttir et al. (2003b)]. Nonetheless, in short, F scales according to $\Omega^{2.6}$ (due to a contact area that changes nonlinearly with scale), whereas F_{static} scales according to Ω^3 . This is why point granular loads are relatively more important at small scales, and static loading is relatively more important at large scales. This has a very interesting implication: the attenuation effects caused by the mass of the load-measuring system at small scales means that the loading behavior may actually be representative of large scales due to compensating error. Indeed, Fig. 14(a) (lab scale) and Fig. 14(b) (field scale) show almost identical normalized impact loading curves.

Figs. 15(a and b) show the effects of changing the scale and the elastic modulus in more detail. Fig. 15(a) corresponds to an

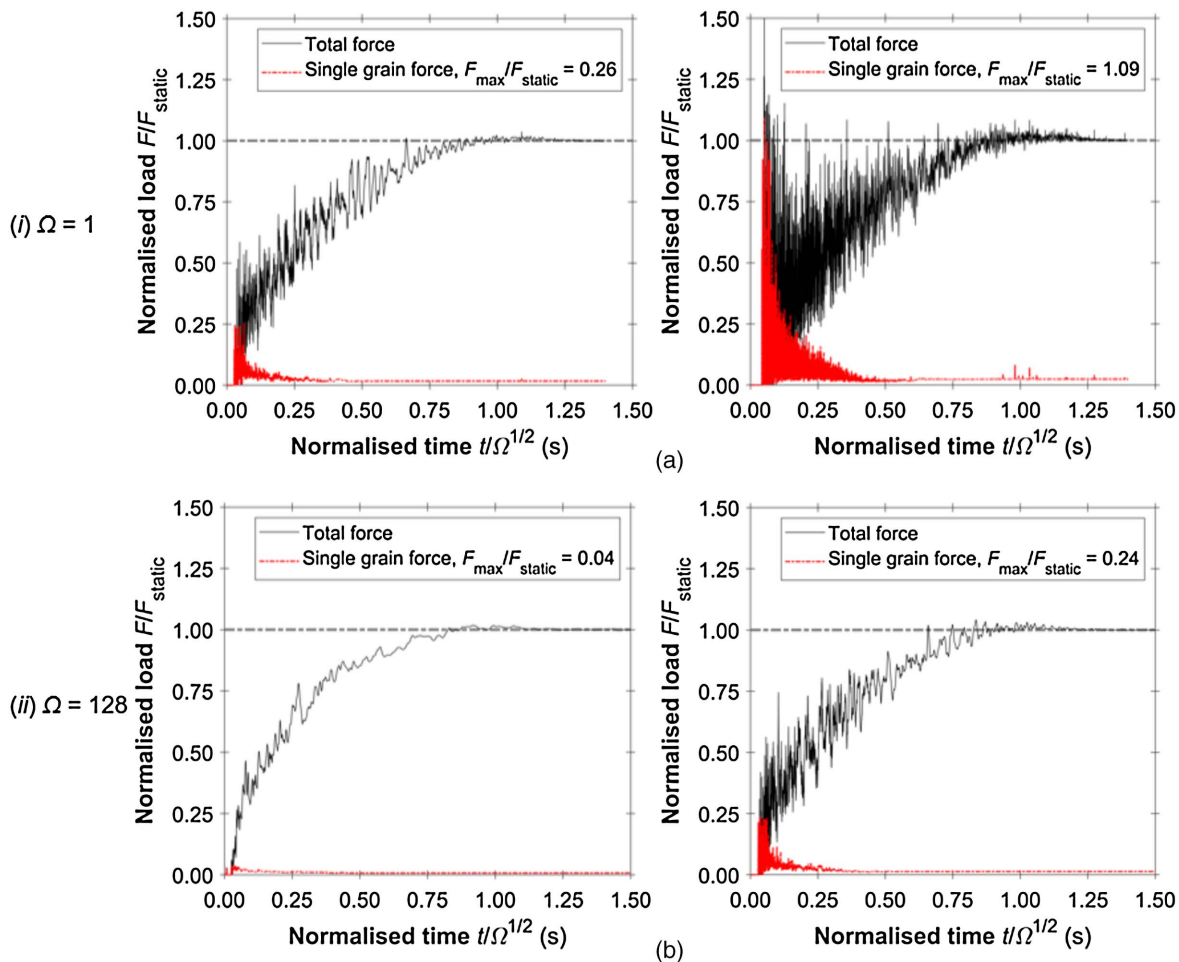


Fig. 14. Impact load-time histories across a range of scales, specifically $\Omega = 1$ and $\Omega = 128$ for elastic moduli $E = 10^8$ and 10^{10} Pa.

elastic moduli $E = 0.1$ GPa (commonly adopted in DEM studies) (Table 2) and Fig. 15(b) corresponds to $E = 10$ GPa (closer to the material elastic modulus for real geological materials). Two lines are shown for each value of E : (1) the highest instantaneous grain load normalized by the final static load; and (2) the maximum load, which can refer to either the maximum grain load due to one or more grains, or the final static load due to the bulk granular assembly. The theoretical lines are calculated using the set of equations described in Appendix II (e.g., Johnson 1985; Zhang et al. 1996; Hákonadóttir et al. 2003b). The trend of F/F_{static} for individual impacts follows the same trend implied by the theory; both the gradient of the slopes and the value of the data points match reasonably.

For the total loading due to the bulk granular assembly, the final static load dominates at every model size for $E = 0.1$ GPa [Fig. 15(a)]. For $E = 10$ GPa [Fig. 15(b)], the maximum total load can be said to be governed by discrete Hertzian loading for $h < 1$ m. For $h < 1$ m, the maximum load due to the bulk assembly is slightly higher than both the maximum load on a single grain and the final static load. This is related to whether concurrent impacts of grains tend to occur; the relative lack of importance of concurrent impacts for this value of E is because the contact duration is very short [Eq. (5) and Leonardi et al. (2014)]. Concurrent impacts also occur for $E = 0.1$ GPa, where, due to the longer impact time, the incidence of concurrent impacts is higher than for $E = 10$ GPa. However, these concurrent impacts are not enough to overcome the final static load and so do not govern the loading behavior.

These results imply that the system of equations presented in Appendix II may give a reasonable indicator as to the governing load for any particular problem. They give a helpful theoretical basis for when boulders can be assumed to be part of the flow and when they should be considered to exert point loads on a barrier. It appears that if hydrostatic scaling is adopted, granular flows impacting barriers are largely scale-independent, but grain impacts based on established Hertzian contact mechanics are not. Nonetheless, other numerical schemes, perhaps based on the hard-soft sphere hybrid method proposed by Buist et al. (2016), may ultimately be more appropriate for modeling the behavior and impact force of the dispersed flow front.

Conclusions

The main novel contributions from this study were to systematically investigate translational inertial effects and scaling considerations for coarse granular flows impacting a load-measuring barrier. This study reveals that there are two main scaling considerations for granular flows impacting load-measuring systems: (1) the design of the load-measuring system, and (2) the scale of the model (e.g., lab scale or full scale):

- Considerations relating to the design of the load-measuring system include the relative masses of the grains and load-measuring system, the equivalent spring element stiffness of the load-measuring system, and the impact velocity of the

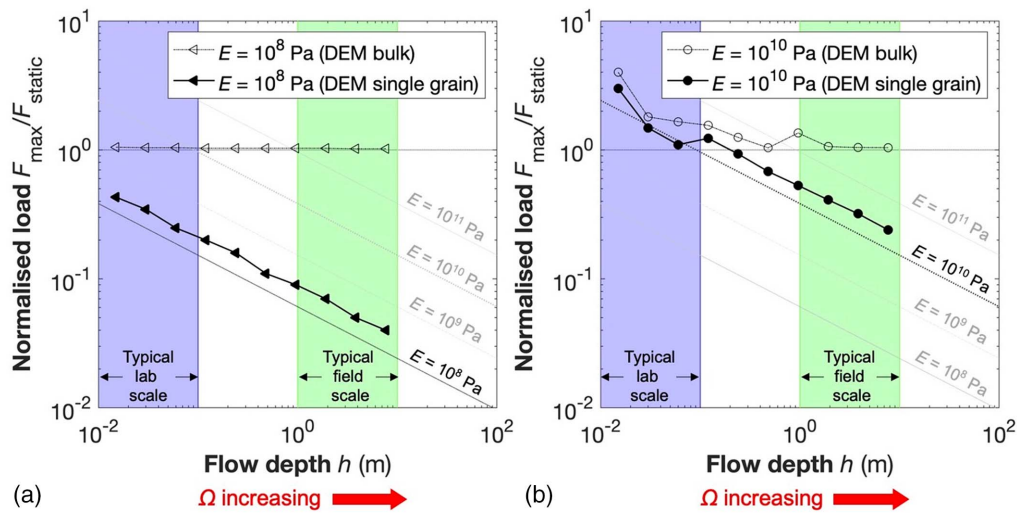


Fig. 15. Ratio of Hertzian and final static loads across a range of scales: (a) $E = 10^8$ Pa; and (b) $E = 10^{10}$ Pa. The straight reference lines are calculated from the set of equations in Appendix II. The regions for scale are nominal ranges based on studies such as those by Choi et al. (2015) and Kessler et al. (2020) for the lab scale. For the field scale, the regions correspond to Iverson (1997) and Iverson and George (2014).

grains. A dimensionless number was proposed and evaluated that describes the extent to which the ratio of masses between a barrier and grains in a flow front influence the measured load. This number considers translational inertia and impact velocity. The number can be used to evaluate the design of physical load-measuring systems to enable a higher degree of load transmission from individual grains.

- It was shown both numerically and theoretically that the impact dynamics for coarse dry granular flows are not scale-independent within the framework of Hertzian contact mechanics. Although the final static load on a barrier scales directly with an increase in the dimensions of a model, discrete Hertzian impacts increase at a lower rate with scale. This implies that discrete impacts become proportionately less important as the model scale is increased.
- It appears that there is beneficial compensating error caused by adopting elastic moduli that are much lower than typical geomaterials (~ 0.1 GPa) as input parameters for DEM simulations of small-scale channelized flows. This is because discrete Hertzian impacts reduce in importance with scale relative to the final static load on a barrier. Using lower elastic moduli for small-scale DEM simulations allows these reduced discrete Hertzian impacts, characteristic of large-scale impact cases, to be modeled at small scales.
- Concurrent impacts are statistically more likely for lower elastic moduli (e.g., $E = 0.1$ GPa), which are probably less relevant for real engineering geomaterials and barrier materials. This indicates that the principle of superposition in some design guidelines (i.e., adding the discrete loads from all the coarse grains at the flow front and treating the total load as the design one) may result in overly conservative design.

Appendix I. Contact Model

Soft-sphere DEM contact models can be linear (e.g., Hookean) or nonlinear (e.g., Hertzian). This affects the way in which the contact force is computed. A Hertzian model was selected in this study because interactions between grains are inherently nonlinear. In the LIGGGHTS implementation of the DEM, the basic governing equation for contact forces between the i th and j th grains F_{ij} is

given as follows (DCS Computing 2020; Brilliantov et al. 1996; Zhang and Makse 2005):

$$F_n + F_t = [k_n \delta \mathbf{n}_{ij} - \gamma_n \mathbf{u} \mathbf{n}_{ij}] + [k_t \delta \mathbf{t}_{ij} - \gamma_t \mathbf{u} \mathbf{t}_{ij}] \quad (12)$$

where k_n and k_t = elastic parameters for normal and tangential contacts, respectively; $\delta \mathbf{n}_{ij}$ and $\delta \mathbf{t}_{ij}$ = distances by which grains overlap normally and tangentially (Silbert et al. 2001); γ_n and γ_t = viscoelastic damping constants for normal and tangential contacts; and $\mathbf{u} \mathbf{n}_{ij}$ and $\mathbf{u} \mathbf{t}_{ij}$ = normal and tangential components of the relative velocity of the two grains. In Hertzian contact models, values for k_n , k_t , γ_n , and γ_t are a function of time-varying parameters such as the overlap distance

$$k_n = \frac{4}{3} E^* \sqrt{r_g \delta \mathbf{n}_{ij}} \quad (13)$$

$$\gamma_n = -2 \sqrt{\frac{5}{6}} \beta(e) \sqrt{2 E^* (r_g^* \delta \mathbf{n}_{ij})^{1/2} m^*} \geq 0 \quad (14)$$

$$k_t = 8 G^* \sqrt{r_g^* \delta \mathbf{n}_{ij}} \quad (15)$$

$$\gamma_t = -2 \sqrt{\frac{5}{6}} \beta(e) \sqrt{8 G^* (r_g^* \delta \mathbf{n}_{ij})^{1/2} m^*} \geq 0 \quad (16)$$

where β = constant that is a function of the coefficient of restitution e .

The effective variables r_g^* , m^* , E^* , and G^* (radius, mass, elastic modulus, and shear modulus, respectively) are given by Eqs. (17)–(20) (e.g., O'Sullivan 2011), and β is given by Eq. (21)

$$\frac{1}{r^*} = \frac{1}{r_1} + \frac{1}{r_2} \quad (17)$$

$$\frac{1}{m^*} = \frac{1}{m_1} + \frac{1}{m_2} \quad (18)$$

$$\frac{1}{E^*} = \frac{(1 - \nu_1^2)}{E_1} + \frac{(1 - \nu_2^2)}{E_2} \quad (19)$$

$$\frac{1}{G^*} = \frac{2(2 - \nu_1^2)(1 + \nu_1^2)}{E_1} + \frac{2(2 - \nu_2^2)(1 + \nu_2^2)}{E_2} \quad (20)$$

$$\beta = \frac{\ln e}{\sqrt{\ln^2 e + \pi^2}} \quad (21)$$

where ν = Poisson's ratio.

For planes modeled using the DEM, the radius and mass are assumed to tend to infinity, meaning that $r^* \rightarrow r$ and $m^* \rightarrow m$. Furthermore, Eq. (19) implies that the effective elastic modulus is governed by the material that is softer. Furthermore, none of the tangential equations are required for normal impact cases, as in the drop tests on a displaceable barrier performed in this study. Nonetheless, frictional forces are important for the granular flows modeled in this study. Finally, the tangential forces in Eq. (17) are subject to the following condition:

$$F_t \leq \phi' F_n \quad (22)$$

where ϕ' = either the intergrain or interface friction angle.

Appendix II. Geometric Scaling Factor Ω

Applying the geometric scaling factor Ω to quantities with length (e.g., the flow depth h_1), the equations from the main text can be modified. To hold Fr constant across different scales, the velocity U_1 must be proportional to $\sqrt{\Omega}$ to ensure that it changes at the same rate as h_1 (which is proportional to Ω)

$$Fr = \frac{U_1 \sqrt{\Omega}}{\sqrt{g(\Omega h_1) \cos \theta}} \quad (23)$$

where g = acceleration due to gravity; and θ = channel inclination. The equation for pileup proposed by Hákonađóttir et al. (2003b) can then be modified to be written

$$\frac{\Omega U_1^2}{\Omega g h_1 \cos \theta} + 1 = \left(\frac{\kappa h_2}{\Omega h_1} \right)^2 - \frac{\kappa h_2}{\Omega h_1} + \left(\frac{\kappa h_2}{\Omega h_1} \right)^{-1} \quad (24)$$

where h_2 = pileup height after impact; and κ = unknown coefficient of proportionality. For $Fr > 1$, it can be shown that $\kappa h_2 = \Omega h_2$, i.e., $\kappa = \Omega$. Eq. (24) behaves nonlinearly for $Fr < 1$, but this nonlinearity is neglected in this analysis because $Fr < 1$ is not typically the most important case to consider for impact. This means that the final static load can be estimated as follows:

$$F_{\text{static}} = \frac{1}{2} (\Omega B \Omega h_2 \cos \theta) (\phi \rho g \Omega h_2 \cos \theta) \quad (25)$$

where ϕ = solid volume fraction; and ρ = bulk density. Eq. (25) shows that $F_{\text{static}} \propto \Omega^3$.

The Hertzian load for a single grain is derived assuming finite overlap from two spheres and can be directly written as follows (e.g., Johnson 1985; Zhang et al. 1996):

$$F_{\text{grain}} = \frac{4}{3} E^* \sqrt{\Omega r_g} \left\{ \frac{15 m(\Omega) [\sqrt{\Omega} U_1]^2}{16 E^* \sqrt{\Omega r_g}} \right\}^{0.6} \quad (26)$$

where $m(\Omega)$ indicates that mass m is some function of Ω because it depends on the grain radius. By writing m explicitly in terms of the grain radius, we obtain

$$F_{\text{grain}} = \frac{4}{3} E^* \sqrt{\Omega r_g} \left\{ \frac{15 \rho \left[\frac{4}{3} \pi (\Omega r_g)^3 \right] [\sqrt{\Omega} U_1]^2}{16 E^* \sqrt{\Omega r_g}} \right\}^{0.6} \quad (27)$$

which can be reduced to show that $F \propto \Omega^{2.6}$.

Data Availability Statement

Some or all data, models, or code that support the findings of this study are available from the corresponding author upon reasonable request. This includes the load cell data and the code used for the DEM simulations, as well as the MATLAB version 2019b code used for data extraction and graph plotting.

Acknowledgments

The authors are grateful for the generous financial sponsorship from the National Natural Science Foundation of China (51709052), as well as the Research Grants Council of Hong Kong (General Research Fund Grant Nos. 16212618, 16209717, 16210219, T22-603/15N, and AoE/E-603/18) and the University of Hong Kong start-up fund for new staff from the Department of Civil Engineering and the Faculty of Engineering. Furthermore, some of the work was performed while the first author was working in France under funding graciously provided as part of the MOPGA 2021–22 scheme (MOPGA-976501H), from the Agence Nationale de la Recherche (France). The authors would also like to thank Mr. Doug Ho for a useful preliminary investigation conducted on DEM contact models for open-channel flows. The authors are also grateful for the detailed comments and suggestions given by two anonymous reviewers, whose input helped to greatly improve the manuscript.

Notation

The following symbols are used in this paper:

- B = channel width;
- D = thickness of load-bearing plate;
- D_t = thickness of load transducer;
- d = elastic deformation or overlap between grains;
- E = Young's modulus;
- E_g = Young's modulus of grain;
- E_1 = Young's modulus of Grain 1;
- E_2 = Young's modulus of Grain 2;
- E^* = effective Young's modulus;
- e = coefficient of restitution;
- F = force or load;
- F_{grain} = force on a grain;
- $F_{\text{grain max}}$ = maximum force on a grain during impact;
- F_{max} = maximum load on a barrier plate;
- F_n = normal force;
- F_{spring} = force in equivalent spring;
- F_{static} = static load on barrier due to pileup;
- F_t = tangential force;
- Fr = Froude number;
- f = frequency of vibration;
- G = shear modulus;
- G^* = effective shear modulus;
- g = acceleration due to gravity;
- H = height of load-bearing plate;
- H_t = height of load-transducer;

h = flow depth;
 h_1 = flow depth before impact;
 h_2 = pileup height after impact;
 I = second moment of area;
 k_g = equivalent linear material stiffness of a grain;
 k_n = normal spring stiffness for DEM;
 k_p = spring element stiffness for plate;
 k_t = tangential spring stiffness for DEM;
 L = distance from gate to barrier;
 L_{beam} = length of beam;
 M = mass of load-measuring system;
 m = mass of grain;
 m_1 = mass of Grain 1;
 m_2 = mass of Grain 2;
 m^* = composite mass of colliding objects;
 r_g = grain radius;
 r_g^* = effective grain radius;
 r_1 = radius of Grain 1;
 r_2 = radius of Grain 2;
 t = time;
 t_g = timescale of the contact time of a grain during impact;
 t_p = timescale of vibration for barrier plate;
 U_{max} = maximum flow velocity;
 U_z = velocity in the z -direction;
 U_1 = grain velocity before impact;
 un_{ij} = normal relative velocity in DEM;
 ut_{ij} = tangential relative velocity in DEM;
 W = width of load-bearing plate;
 W_t = width of load-transducer;
 x_z = displacement in the z -direction;
 β = constant depending on coefficient of restitution e ;
 γ_n = normal damping value for DEM;
 γ_p = damping constant for load-measuring system;
 γ_t = tangential damping value for DEM;
 Γ = dimensionless number describing proportion of load measured by a load-cell transducer;
 δ = grain diameter;
 δ_{max} = maximum grain diameter;
 δ_{min} = minimum grain diameter;
 δn_{ij} = normal overlap in DEM;
 δt_{ij} = tangential overlap in DEM;
 θ = channel inclination;
 κ = coefficient of proportionality;
 ν_g = Poisson's ratio for grains;
 ν_1 = Poisson's ratio of grain # 1;
 ν_2 = Poisson's ratio of grain # 2;
 ρ = material density;
 ϕ' = friction angle; and
 Ω = geometric scaling factor.

References

- Albaba, A., S. Lambert, and T. Faug. 2018. "Dry granular avalanche force on a rigid wall: analytic shock solution versus discrete element simulations." *Phys. Rev. E* 97 (5): 052903. <https://doi.org/10.1103/PhysRevE.97.052903>.
- Albaba, A., S. Lambert, F. Nicot, and B. Chareyre. 2015. "Relation between microstructure and loading applied by a granular flow to a rigid wall using DEM modelling." *Granular Matter* 17 (5): 603–616. <https://doi.org/10.1007/s10035-015-0579-8>.
- An, B., and D. D. Tannant. 2007. "Discrete element method contact model for dynamic simulation of inelastic rock impact." *Comput. Geosci.* 33 (4): 513–521. <https://doi.org/10.1016/j.cageo.2006.07.006>.
- Antypov, D., and J. A. Elliott. 2011. "On an analytical solution for the damped Hertzian spring." *Europhys. Lett.* 94 (5): 50004. <https://doi.org/10.1209/0295-5075/94/50004>.
- Armanini, A. 2015. "Closure relations for mobile bed debris flows in a wide range of slopes and concentrations." *Adv. Water Resour.* 81 (Jul): 75–83. <https://doi.org/10.1016/j.advwatres.2014.11.003>.
- Armanini, A., M. Larcher, E. Nucci, and M. Dumbser. 2014. "Submerged granular channel flows driven by gravity." *Adv. Water Resour.* 63 (Jan): 1–10. <https://doi.org/10.1016/j.advwatres.2013.10.007>.
- Armanini, A., M. Larcher, and M. Odorizzi. 2011. "Dynamic impact of debris flow front against a vertical wall." In *Proc., 5th Int. Conf. on Debris-Flow Hazards Mitigation: Mechanics, Prediction and Assessment 2011*, 1041–1049. Rome: Casa Editrice Università La Sapienza.
- Ashwood, W., and O. Hungr. 2016. "Estimating total resisting force in flexible barrier impacted by a granular avalanche using physical and numerical modelling." *Can. Geotech. J.* 53 (10): 1700–1717. <https://doi.org/10.1139/cgj-2015-0481>.
- Baselt, I., G. Q. de Oliveira, J.-T. Fischer, and S. P. Pudasaini. 2021. "Evolution of stony debris flows in laboratory experiments." *Geomorphology* 372 (Jan): 107431. <https://doi.org/10.1016/j.geomorph.2020.107431>.
- Brilliantov, N. V., F. Spahn, J.-M. Hertzsch, and T. Pöschel. 1996. "Model for collisions in granular gases." *Phys. Rev. E* 53 (5): 5382–5392. <https://doi.org/10.1103/PhysRevE.53.5382>.
- Bugnion, L., B. W. McArdell, P. Bartelt, and C. Wendeler. 2012. "Measurements of hillslope debris flow impact pressure on obstacles." *Landslides* 9 (2): 179–187. <https://doi.org/10.1007/s10346-011-0294-4>.
- Buist, K. A., L. J. H. Seelen, N. G. Deen, J. T. Padding, and J. A. M. Kuipers. 2016. "On an efficient hybrid soft and hard sphere collision integration scheme for DEM." *Chem. Eng. Sci.* 153 (Oct): 363–373. <https://doi.org/10.1016/j.ces.2016.07.030>.
- Caccamo, P., B. Chanut, T. Faug, H. Bellot, and F. Naaim-Bouvet. 2012. "Small-scale tests to investigate the dynamics of finite-sized dry granular avalanches and forces on a wall-like obstacle." *Granular Matter* 14 (5): 577–587. <https://doi.org/10.1007/s10035-012-0358-8>.
- Canelli, L., A. M. Ferrero, M. Migliazza, and A. Segalini. 2012. "Debris flow risk mitigation by the means of rigid and flexible barriers—experimental tests and impact analysis." *Nat. Hazards Earth Syst. Sci.* 12 (5): 1693–1699. <https://doi.org/10.5194/nhess-12-1693-2012>.
- Chau, K. T., R. H. C. Wong, and C. F. Lee. 1998. "Rockfall problems in Hong Kong and some new experimental results for coefficients of restitution." *Int. J. Rock Mech. Min. Sci. Geomech.* 35 (4–5): 662–663.
- Choi, C. E., S. C. H. Au-Yeung, C. W. W. Ng, and D. Song. 2015. "Flume investigation of landslide granular debris and water runoff mechanisms." *Geotech. Lett.* 5 (1): 28–32. <https://doi.org/10.1680/geolett.14.00080>.
- Choi, C. E., G. R. Goodwin, C. W. W. Ng, D. K. H. Cheung, J. S. H. Kwan, and W. K. Pun. 2016. "Coarse granular flow interaction with slit-structures." *Geotech. Lett.* 6 (4): 267–274. <https://doi.org/10.1680/jgele.16.00103>.
- Christoforou, A. P., A. S. Yigit, and M. Majeed. 2013. "Low-velocity impact response of structures with local plastic deformation: characterisation and scaling." *J. Comput. Nonlinear Dyn.* 8 (1): 011012. <https://doi.org/10.1115/1.4006532>.
- Coetzee, C. J. 2017. "Review: Calibration of the discrete element method." *Powder Technol.* 310 (Apr): 104–142. <https://doi.org/10.1016/j.powtec.2017.01.015>.
- Cui, Y., C. E. Choi, L. H. D. Liu, and C. W. W. Ng. 2018. "Effects of particle size of mono-disperse granular flows impacting a rigid barrier." *Nat. Hazards* 91 (3): 1179–1201. <https://doi.org/10.1007/s11069-018-3185-3>.
- Cundall, P. A., and O. D. L. Strack. 1979. "A discrete numerical model for granular assemblies." *Géotechnique* 29 (1): 47–65. <https://doi.org/10.1680/geot.1979.29.1.47>.
- DCS Computing. 2020. *LIGGGHTS user manual: Gran model*. Linz, Austria: DCS Computing.

- Faug, T., P. Caccamo, and B. Chanut. 2011. "Equation for the force experienced by a wall overflowed by a granular avalanche: Experimental verification." *Phys. Rev. E* 84 (5): 051301. <https://doi.org/10.1103/PhysRevE.84.051301>.
- Faug, T., P. Gauer, K. Lied, and M. Naaim. 2008. "Overrun length of avalanches overtopping catching dams: Cross-comparison of small-scale laboratory experiments and observations from full-scale avalanches." *J. Geophys. Res. Earth Surf.* 113 (F3): F03009. <https://doi.org/10.1029/2007JF000854>.
- Faug, T., P. Lachamp, and M. Naaim. 2002. "Experimental investigation on steady granular flows interacting with an obstacle down an inclined channel: study of the dead-zone upstream from the obstacle. application to interaction between dense snow avalanches and defence structures." *Nat. Hazards Earth Syst. Sci.* 2 (3–4): 187–191. <https://doi.org/10.5194/nhess-2-187-2002>.
- Faug, T., M. Naaim, D. Bertrand, and P. Lachamp. 2003. "Varying dam height to shorten the run-out of dense avalanche flows: developing a scaling law from laboratory experiments." *Surv. Geophys.* 24 (5–6): 555–568. <https://doi.org/10.1023/B:GEOP.000006082.64341.80>.
- Goodwin, G. R., and C. E. Choi. 2020. "Slit structures: Fundamental mechanisms of mechanical trapping of granular flows." *Comput. Geotech.* 119 (Mar): 103376. <https://doi.org/10.1016/j.compgeo.2019.103376>.
- Goodwin, G. R., C. E. Choi, and C.-Y. Yune. 2021. "Towards rational use of baffle arrays on sloped and horizontal terrain for filtering boulders." *Can. Geotech. J.* <https://doi.org/10.1139/cgj-2020-0363>.
- Gray, J. M. N. T., Y. C. Tai, and S. Noelle. 2003. "Shock waves, dead-zones and particle-free regions in rapid granular free-surface flows." *J. Fluid Mech.* 491 (Sep): 161–181. <https://doi.org/10.1017/S0022112003005317>.
- Hákonadóttir, K. M., A. J. Hogg, J. Batey, and A. W. Woods. 2003a. "Flying avalanches." *Geophys. Res. Lett.* 30 (23): 2191. <https://doi.org/10.1029/2003GL018172>.
- Hákonadóttir, K. M., A. J. Hogg, and T. Jóhannesson. 2003b. *A laboratory study of the interaction between supercritical shallow flows and dams*. Rep. No. 03038. Reykjavík, Iceland: Icelandic Meteorological Office.
- Hübl, J., J. Suda, and D. Proske. 2009. "Debris flow impact estimation steep slopes." In Vol. 1 of *Proc., 11th Int. Symp. on Water Management and Hydraulic Engineering*, 137–148. Skopje, Macedonia, Faculty of Civil Engineering, Univ. od Ss Cyril and Methodius.
- Hungr, O., and S. G. Evans. 1988. "Engineering evaluation of fragmental rockfall hazards." In *Proc., 5th Int. Symp. on Landslides*, 685–690. Rotterdam, Netherlands: CRC Press.
- Ishikawa, N., R. Inoue, M. Beppu, Y. Hasegawa, and T. Mizuyama. 2010. "Dynamic load characteristics of debris flow model using different gravel size distribution." In *Proc., INTERPRAEVENT*, 207–216. Taipei, Taiwan: International Research Society.
- Iverson, R. M. 1997. "The physics of debris flows." *Rev. Geophys.* 35 (3): 245–296. <https://doi.org/10.1029/97RG00426>.
- Iverson, R. M. 2015. "Scaling and design of landslide and debris-flow experiments." *Geomorphology* 244 (Mar): 9–20. <https://doi.org/10.1016/j.geomorph.2015.02.033>.
- Iverson, R. M., and D. L. George. 2014. "A depth-averaged debris-flow model that includes the effects of evolving dilatancy. I. Physical basis." *Proc. R. Soc.: Math. Phys. Eng. Sci.* 470 (2170): 20130819. <https://doi.org/10.1098/rspa.2013.0819>.
- Iverson, R. M., M. Logan, R. LaHusen, and M. Berti. 2010. "The perfect debris flow? Aggregated results from 28 large scale experiments." *J. Geophys. Res.: Earth Sci.* 115: F03005. <https://doi.org/10.1029/2009JF001514>.
- Jiang, Y., and I. Towhata. 2013. "Experimental study of dry granular flow and impact behavior against a rigid retaining wall." *Rock Mech. Rock Eng.* 46 (4): 713–729. <https://doi.org/10.1007/s00603-012-0293-3>.
- Jóhannesson, T., P. Gauer, D. Issler, and K. Lied. 2009. *The design of avalanche protection dams recent practical and theoretical developments*. Brussels, Belgium: European Commission.
- Johnson, K. L. 1985. *Contact mechanics*. Cambridge, UK: Cambridge University Press.
- Jop, P., Y. Forterre, and O. Pouliquen. 2006. "A constitutive law for dense granular flows." *Nature* 441 (7094): 727–730. <https://doi.org/10.1038/nature04801>.
- Kessler, M., V. Heller, and B. Turnbull. 2020. "Grain Reynolds number scale effects in dry granular slides." *J. Geophys. Res. Earth Surf. (AGU)* 125 (1): e2019JF005347. <https://doi.org/10.1029/2019JF005347>.
- Kloss, C., and C. Goniva. 2010. "LIGGGHTS—A new open source discrete element simulation software." In *Proc., 5th Int. Conf. on Discrete Element Methods*, 25–26. London: Queen Mary Univ. of London.
- Kluger, J. M., T. Sapsis, and A. H. Slocum. 2016. "A high-resolution and large force-range load cell by means of nonlinear cantilever beams." *Precis. Eng.* 43 (Jan): 241–256. <https://doi.org/10.1016/j.precisioneng.2015.08.003>.
- Kneib, F., T. Faug, F. Dufour, and M. Naaim. 2016. "Numerical investigations of the force experienced by a wall subject to granular lid-driven flows: Regimes and scaling of the mean force." *Comput. Particle Mech.* 3 (3): 293–302. <https://doi.org/10.1007/s40571-015-0060-9>.
- Kneib, F., T. Faug, F. Dufour, and M. Naaim. 2019. "Mean force and fluctuations on a wall immersed in a sheared granular flow." *Phys. Rev. E* 99 (5): 052901. <https://doi.org/10.1103/PhysRevE.99.052901>.
- Kneib, F., T. Faug, G. Nicolet, N. Eckert, and M. Naaim. 2019. "Force fluctuations on a wall in interaction with a granular lid-driven cavity flow." *Phys. Rev. E* 96 (4): 042906. <https://doi.org/10.1103/PhysRevE.96.042906>.
- Kumaran, V., and S. Bharathraj. 2013. "The effect of base roughness on the development of a dense granular flow down an inclined plane." *Phys. Fluids* 25 (7): 070604. <https://doi.org/10.1063/1.4812806>.
- Kwan, J. S. H. 2012. *Supplementary technical guidance on design of rigid debris-resisting barriers*. Technical Note No. TN 2/2012. Hong Kong Special Administrative Region, People's Republic of China: HKSAR Government.
- Lam, C., C. Y. Yong, J. S. H. Kwan, and N. T. K. Lam. 2018a. "Overturning stability of l-shaped rigid barriers subjected to rockfall impacts." *Landslides* 15 (7): 1347–1357. <https://doi.org/10.1007/s10346-018-0957-5>.
- Lam, N. T. K., A. C. Y. Yong, C. Lam, J. S. H. Kwan, J. S. Perera, M. M. Disfani, and E. Gad. 2018b. "Displacement-based approach for the assessment of overturning stability of rectangular rigid barriers subjected to point impact." *J. Eng. Mech.* 144 (2): 04017161. [https://doi.org/10.1061/\(ASCE\)JEM.1943-7889.0001383](https://doi.org/10.1061/(ASCE)JEM.1943-7889.0001383).
- Law, R. P. H., C. E. Choi, and C. W. W. Ng. 2015. "Discrete element investigation of the influence of granular debris flow baffles on rigid barrier impact." *Can. Geotech. J.* 53 (2): 179–185.
- Leonardi, A., G. R. Goodwin, and M. Pirulli. 2019. "The force exerted by granular flows on slit dams." *Acta Geotech.* 14 (6): 1949–1963. <https://doi.org/10.1007/s11440-019-00842-6>.
- Leonardi, A., F. K. Wittel, M. Mendoza, and H. J. Herrmann. 2014. "Coupled DEM-LBM method for the free-surface simulation of heterogeneous suspensions." *Comput. Particle Mech.* 1 (1): 3–13. <https://doi.org/10.1007/s40571-014-0001-z>.
- Leonardi, A., F. K. Wittel, M. Mendoza, R. Vetter, and H. J. Herrmann. 2016. "Particle-fluid-structure interaction for debris flow impact on flexible barriers." *Comput. Aided Civ. Infrastruct. Eng.* 31 (5): 323–333. <https://doi.org/10.1111/mice.12165>.
- Mancarella, D., and O. Hungr. 2010. "Analysis of runup of granular avalanches against steep, adverse slopes and protective barriers." *Can. Geotech. J.* 47 (8): 827–841. <https://doi.org/10.1139/T09-143>.
- Maranzano, B. J., and B. C. Hancock. 2016. "Quantitative analysis of impact measurements using dynamic load cells." *Sens. Bio-Sens. Res.* 7 (Mar): 31–37. <https://doi.org/10.1016/j.sbsr.2015.11.005>.
- Marchelli, M., A. Leonardi, M. Pirulli, and C. Scavia. 2019. "On the efficiency of slit-check dams in retaining granular flows." *Géotechnique* 70 (3): 226–237. <https://doi.org/10.1680/jgeot.18.P.044>.
- Marin, F., A. Rohatgi, and S. Charlot. 2017. "WebPlotDigitizer, a polyvalent and free software to extract spectra from old astronomical publications: Application to ultraviolet spectropolarim." In *Instrumentation and methods for astrophysics*. New York: Cornell Univ.
- Moriguchi, S., R. I. Borja, A. Yashima, and K. Sawada. 2009. "Estimating the impact force generated by granular flow on a rigid obstruction." *Acta Geotech.* 4 (1): 57–71. <https://doi.org/10.1007/s11440-009-0084-5>.
- Murdoch, N., P. Michel, D. C. Richardson, K. Nordstrom, C. R. Berardi, S. F. Green, and W. Losert. 2012. "Numerical simulations of granular

- dynamics II: Particle dynamics in a shaken granular material." *Icarus* 219 (1): 321–335. <https://doi.org/10.1016/j.icarus.2012.03.006>.
- Naaim-Bouvet, F., M. Naaim, and T. Faug. 2004. "Dense and powder avalanches: Momentum reduction generated by a dam." *Ann. Glaciol.* 38: 373–378. <https://doi.org/10.3189/172756404781815185>.
- Ng, C. W. W., C. E. Choi, and G. R. Goodwin. 2019. "Froude characterisation for unsteady single-surge dry granular flows: impact pressure and runup height." *Can. Geotech. J.* 56 (12): 1968–1978. <https://doi.org/10.1139/cgj-2018-0529>.
- Ng, C. W. W., C. E. Choi, G. R. Goodwin, and W. Cheung. 2017. "Interaction between dry granular flow and deflectors." *Landslides* 14 (4): 1375–1387. <https://doi.org/10.1007/s10346-016-0794-3>.
- Ng, C. W. W., C. E. Choi, R. C. H. Koo, G. R. Goodwin, D. Song, and J. S. H. Kwan. 2018a. "Dry granular flow interaction with dual-barrier systems." *Géotechnique* 68 (5): 386–399. <https://doi.org/10.1680/jgeot.16.P273>.
- Ng, C. W. W., H. Liu, C. E. Choi, J. S. H. Kwan, and W. K. Pun. 2021. "Impact dynamics of boulder-enriched debris flow on a rigid barrier." *J. Geotech. Geoenviron. Eng.* 147 (3): 04021004. [https://doi.org/10.1061/\(ASCE\)GT.1943-5606.0002485](https://doi.org/10.1061/(ASCE)GT.1943-5606.0002485).
- Ng, C. W. W., D. Song, C. E. Choi, L. H. D. Liu, J. S. H. Kwan, R. C. H. Koo, and W. K. Pun. 2016. "Impact mechanisms of granular and viscous flows on rigid and flexible barriers." *Can. Geotech. J.* 54 (2): 188–206. <https://doi.org/10.1139/cgj-2016-0128>.
- Ng, C. W. W., A. Y. Su, C. E. Choi, C. Lam, J. S. H. Kwan, R. Chen, and H. Liu. 2018b. "Comparison of cushion mechanisms between cellular glass and gabions subjected to successive boulder impacts." *J. Geotech. Geoenviron. Eng.* 144 (9): 04018058. [https://doi.org/10.1061/\(ASCE\)GT.1943-5606.0001922](https://doi.org/10.1061/(ASCE)GT.1943-5606.0001922).
- NILIM (National Institute for Land and Infrastructure Management). 2007. *Manual of technical standard for establishing sabo master plan for debris flow and driftwood*. Technical Note (NILIM) No. 364. Tsukuba, Japan: NILIM.
- O'Sullivan, C. 2011. *Particulate discrete element modelling: A mechanics perspective*. Boca Raton, FL: CRC Press.
- Piton, G., and A. Recking. 2016a. "Design of sediment traps with open check dams. I: Hydraulic and deposition processes." *J. Hydraul. Eng.* 142 (2): 04015045. [https://doi.org/10.1061/\(ASCE\)HY.1943-7900.0001048](https://doi.org/10.1061/(ASCE)HY.1943-7900.0001048).
- Piton, G., and A. Recking. 2016b. "Design of sediment traps with open check dams. II: Woody debris." *J. Hydraul. Eng.* 142 (2): 04015046. [https://doi.org/10.1061/\(ASCE\)HY.1943-7900.0001049](https://doi.org/10.1061/(ASCE)HY.1943-7900.0001049).
- Pudasaini, S. P., K. Hutter, S.-S. Hsiau, S.-C. Tai, Y. Wang, and R. Katzenbach. 2007. "Rapid flow of dry granular materials down inclined chutes impinging on rigid walls." *Phys. Fluids* 19 (5): 053302. <https://doi.org/10.1063/1.2726885>.
- Richardson, D. C., K. J. Walsh, N. Murdoch, and P. Michel. 2011. "Numerical simulations of granular dynamics: I. Hard-sphere discrete element method and tests." *Icarus* 212 (1): 427–437. <https://doi.org/10.1016/j.icarus.2010.11.030>.
- Salciarini, D., C. Tamagnini, and P. Conversini. 2010. "Discrete element modelling of debris-avalanche impact on earthfill barriers." *Phys. Chem. Earth* 35 (3–5): 172–181. <https://doi.org/10.1016/j.pce.2009.05.002>.
- Sandeep, C. S., K. Senetakis, D. K. H. Cheung, C. E. Choi, Y. Wang, M. R. Coop, and C. W. W. Ng. 2020. "Experimental study on the coefficient of restitution of grain against block interfaces for natural and engineered materials." *Can. Geotech. J.* 58 (1): 35–48. <https://doi.org/10.1139/cgj-2018-0712>.
- Scheidl, C., M. Chiari, R. Kaitna, M. Müllegger, A. Krawtschuk, T. Zimmermann, and D. Proske. 2013. "Analysing debris-flow impact models, based on a small scale modelling approach." *Surv. Geophys.* 34 (1): 121–140. <https://doi.org/10.1007/s10712-012-9199-6>.
- Shan, T., and J. Zhao. 2014. "A coupled CFD-DEM analysis of granular flow impacting on water reservoir." *Acta Mech.* 225 (8): 2449–2470. <https://doi.org/10.1007/s00707-014-1119-z>.
- Sheih, C. L., C. H. Ting, and W. Pan. 2008. "Impulsive force of debris flow on a curved dam." *Int. J. Sediment Res.* 23 (2): 149–158. [https://doi.org/10.1016/S1001-6279\(08\)60014-1](https://doi.org/10.1016/S1001-6279(08)60014-1).
- Shen, W., T. Zhao, J. Zhao, F. Dai, and G. D. D. Zhou. 2018. "Quantifying the impact of dry debris flow against a rigid barrier by DEM analyses." *Eng. Geol.* 241 (Jul): 86–96. <https://doi.org/10.1016/j.enggeo.2018.05.011>.
- Silbert, L. E., D. Ertas, G. S. Grest, T. C. Halsey, D. Levine, and S. J. Plimpton. 2001. "Granular flow down an inclined plane: Bagnold scaling and rheology." *Phys. Rev. E* 64 (5): 051302. <https://doi.org/10.1103/PhysRevE.64.051302>.
- Song, D. 2016. "Mechanisms of debris flow impact on rigid and flexible barriers." Ph.D. thesis, Dept. of Civil and Environmental Engineering, Hong Kong Univ. of Science and Technology.
- Song, D., C. E. Choi, G. G. D. Zhou, J. S. H. Kwan, and H. Y. Sze. 2018. "Impulse load characteristics of boulder debris flow impact." *Géotech. Lett.* 8 (2): 111–117. <https://doi.org/10.1680/jgele.17.00159>.
- Song, D., C. W. W. Ng, C. E. Choi, G. G. D. Zhou, J. S. H. Kwan, and R. C. H. Koo. 2017. "Influence of debris flow solid fraction on rigid barrier impact." *Can. Geotech. J.* 54 (10): 1421–1434. <https://doi.org/10.1139/cgj-2016-0502>.
- Spadari, M., A. Glacolini, O. Buzzi, and J. P. Hambleton. 2012. "Prediction of the bullet effect for rockfall barriers: A scaling approach." *Rock Mech. Rock Eng.* 45 (2): 131–144. <https://doi.org/10.1007/s00603-011-0203-0>.
- Stratton, R., and C. Wensrich. 2010. "Modelling of multiple intra-time step collisions in the hard-sphere discrete element method." *Powder Technol.* 199 (2): 120–130. <https://doi.org/10.1016/j.powtec.2009.12.008>.
- Su, Y., C. E. Choi, C. W. W. Ng, C. Lam, J. S. H. Kwan, G. Wu, J. Huang, and Z. Zhang. 2018. "Eco-friendly recycled crushed glass for cushioning boulder impacts." *Can. Geotech. J.* 56 (9): 1251–1260. <https://doi.org/10.1139/cgj-2018-0200>.
- Su, Y., Y. Cui, C. W. W. Ng, C. E. Choi, and J. S. H. Kwan. 2017. "Effects of particle size and cushioning thickness on the performance of rock-filled gabions used in protection against boulder impact." *Can. Geotech. J.* 56 (2): 198–207. <https://doi.org/10.1139/cgj-2017-0370>.
- Tan, D., J. Yin, W. Feng, Z. Zhu, J. Qin, and W. Chen. 2020. "New simple method for calculating impact force on flexible barrier considering partial muddy debris flow passing through." *J. Geotech. Geoenviron. Eng.* 145 (9): 04019051. [https://doi.org/10.1061/\(ASCE\)GT.1943-5606.0002133](https://doi.org/10.1061/(ASCE)GT.1943-5606.0002133).
- Teufelsbauer, H., Y. Wang, M.-C. Chiou, and W. Wu. 2009. "Flow-obstacle-interaction in rapid granular avalanches: DEM simulation and comparison with experiment." *Granular Matter* 11 (4): 209–220. <https://doi.org/10.1007/s10035-009-0142-6>.
- Teufelsbauer, H., Y. Wang, S. P. Pudasaini, R. I. Borja, and W. Wu. 2011. "DEM simulation of impact force exerted by granular flow on rigid structures." *Acta Geotech.* 6 (3): 119–133. <https://doi.org/10.1007/s11440-011-0140-9>.
- Thielicke, W., and E. J. Stamhuis. 2014. "PIVlab-time-resolved digital particle image velocimetry tool for MATLAB." *J. Open Res. Software* 2 (1): 1–10. <https://doi.org/10.5334/jors.bl>.
- Tiberghien, D., D. Laigle, M. Naaim, E. Thibert, and F. Ousset. 2007. "Experimental investigation of interaction between mudflow and obstacle." In *Debris-flow hazards mitigation: Mechanics, prediction and assessment*, edited by C. Chen and J. J. Major, 281–292. Rotterdam, Netherlands: Millpress Science Publishers.
- Vagnon, F., and A. Segalini. 2016. "Debris flow impact estimation on a rigid barrier." *Nat. Hazards Earth Syst. Sci.* 16 (7): 1691–1697. <https://doi.org/10.5194/nhess-16-1691-2016>.
- WSL (Wald, Schnee und Landschaft). 2008. *Integral risk management of extremely rapid mass movements*. Technical Note (NILIM) No. 364. Birmensdorf, Switzerland: WSL.
- Yigit, A. S., A. P. Christoforou, and M. A. Majeed. 2011. "A nonlinear visco-elastoplastic impact model and the coefficient of restitution." *Nonlinear Dyn.* 66 (4): 509–521. <https://doi.org/10.1007/s11071-010-9929-6>.
- Yong, A. C. Y., C. Lam, N. T. K. Lam, and J. S. Perera. 2019. "Analytical solution for estimating sliding displacement of rigid barriers subjected to boulder impact." *J. Eng. Mech.* 145 (3): 04019006. [https://doi.org/10.1061/\(ASCE\)EM.1943-7889.0001576](https://doi.org/10.1061/(ASCE)EM.1943-7889.0001576).

Zhang, B., and Y. Huang. 2021. "Unsteady overflow behavior of polydisperse granular flows against closed type barrier." *Eng. Geol.* 280 (Jan): 105959. <https://doi.org/10.1016/j.enggeo.2020.105959>.

Zhang, H. P., and H. A. Makse. 2005. "Jamming transition in emulsions and granular materials." *Phys. Rev. E* 72 (1): 011301. <https://doi.org/10.1103/PhysRevE.72.011301>.

Zhang, S., O. Hungr, and O. Slaymaker. 1996. "The calculation of impact force of boulders in debris flow." In *Debris flow observation and research*, edited by R. Du. Beijing: Science Press.

Zhou, G. G. D., and C. W. W. Ng. 2010. "Numerical investigation of reverse segregation in debris flows by DEM." *Granular Matter* 12 (5): 507–516. <https://doi.org/10.1007/s10035-010-0209-4>.